Check for updates

# Design of pre-catalysts for heterogeneous CO$_2$ electrochemical reduction

Jingfu He, [ID] * Chenghui Wu, Yanming Li and Changli Li [ID] *

CO$_2$ reduction reaction (CO$_2$RR) is one of the most promising methods to alleviate the global challenge of climate change and energy supply. Metal catalysts such as copper, gold, silver, tin, bismuth, *etc.*, attract great attention for their high efficiency to convert CO$_2$ into valuable chemicals such as CO, HCOOH, C$_2$H$_4$ and C$_2$H$_5$OH. It is of interest that the unstable metal-based compounds can be considered as pre-catalysts due to the *in situ* formation of a metallic state during CO$_2$RR, resulting in a reconstruction of surface catalytic structures that mediate much higher CO$_2$RR activity than their metal foil counterparts. However, the precise evolution process of the catalysts during CO$_2$RR and ultimate active sites of the catalyst have not been fully tracked and determined. In this review, we summarize the recent development of metal oxides, metal dichalcogenides, metal halides, metal nitrides and metal–organic compound pre-catalysts, and focus on the structural evolution during the activation process. The key structural factors that impact the performance of catalysts are analyzed in-depth in terms of the remnant of anion elements, enhanced surface areas, facet orientation, and grain boundaries. A perspective is also provided to tackle the critical challenges in designing highly efficient CO$_2$RR pre-catalysts, including the manipulation and identification of surface roughness, structure disorder and partial oxidation of metal center, the monitoring and regeneration of catalysts under a long-time operation, the elimination of impurities during operation and fine control of multicomponent for structural regulation.

## 1. Introduction

The development of (photo)electrochemical methods to harvest renewable energy and produce valuable chemical fuels is a key step to build a sustainable society.[1-5] Electrochemical CO$_2$ reduction (CO$_2$RR) that utilizes clean electricity to complete carbon fixation and synthesize fuel is an effective way to alleviate the energy and environmental crisis.[6-9] To realize industrialized electrochemical CO$_2$ reduction, it is necessary to optimize the construction of an electrochemical system so that it can catalytically reduce CO$_2$ into a single product with high energy conversion efficiency and high selectivity. CO$_2$ reduction is a very complex reaction with a series of products with very

*School of Materials, Sun Yat-sen University, Guangzhou 510275, Guangdong, P. R. China. E-mail: hejf27@mail.sysu.edu.cn; lichli5@mail.sysu.edu.cn*

*Jingfu He is currently an associate professor in School of Materials, Sun Yat-sen University. He received his Ph.D. in 2012 from University of Science and Technology of China. He joined the Berlinguette group at the University of British Columbia as a postdoctoral associate in 2015 and conducted research on film synthesis and CO$_2$ electrocatalysis. His current research interests include photoelectrochemistry and electrochemistry for CO$_2$ reduction, water splitting and in situ synchrotron radiation spectrum.*

*Changli Li is an Associate Professor at the School of Materials, Sun Yat-sen University, China. He received his PhD degree in Mechanical Engineering from The University of Tokyo, Japan, in 2015. After Post-Doctoral studies at Tsinghua University and The University of British Columbia, he began his independent career as a faculty member at Sun Yat-sen University. His research activities focus on the synthesis of nanostructured materials and semiconductor heterojunctions for electrochemical and photoelectrochemical energy conversion.*

close electrode potentials.[10,11] In addition, the side reaction of hydrogen evolution is difficult to avoid, because the electrode potential of $CO_2$ reduction is very close to that of hydrogen evolution. These difficulties have made the research of catalysts one of the most restrictive factors for $CO_2$RR industrialization.

It is generally believed that the initial reduction of $CO_2$ can be roughly divided into two pathways, one is to generate formic acid, and the other is to generate CO.[12] Formic acid cannot be further reduced in this reducing environment. On the other hand, CO may continue to be adsorbed on the surface of the catalyst and be deeply reduced to a series of products, such as methane, ethylene, ethanol, and acetic acid. The reaction pathway and termination of $CO_2$RR is determined by the surface electron and atomic structure of the catalyst, which determines the ability of the catalyst to combine with a series of intermediate products.

Previous research on single metal has classified metals into several groups with different catalytic selectivity.[10,12,13] The most inert metals that difficult to form M–C bond, such as lead, mercury, tin and indium, mainly produce formic acid. Metals with weak CO adsorption strength, such as gold and silver, produce CO as the final reduction product. Metals with very strong CO adsorption strength, such as iron, cobalt, nickel, platinum, *etc.*, are vulnerable to the surface poisoning, resulting in the production of hydrogen. The interaction between Cu and CO is moderate, thus it is the only catalyst that can further reduce CO. However, the Cu catalytic selectivity is very sensitive to the subtle changes in the electronic structure of the surface atoms. For example, the catalytic selectivity of the (111) facet and the (110) facet of copper are significantly different.[14,15] Nevertheless, for the study based on planar metal catalysts, the overall reaction rate is low, and the side reaction of hydrogen production is very strong.

Kanan research group first proposed an oxidation–reduction strategy and found that the $CuO_x$, $AuO_x$ and other metals oxides can be utilized as pre-catalysts, resulting in the formation of nanostructured morphologies with a large number of grain boundaries and a large specific surface area.[16–19] The overall overpotential for $CO_2$RR is reduced by 400 mV compared to the planar electrode, and hydrogen production is greatly suppressed. Smith's group studied OD-Ag for $CO_2$RR and also observed a substantial increase in energy conversion and selectivity.[20,21] After that, the OD strategy has been widely used in various $CO_2$RR metal catalysts.[22–25]

In recent years, other metal–nonmetal compound pre-catalysts, such as metal dichalcogenide, metal nitrite, metal halogens and MOF, were developed as promising pre-catalysts for $CO_2$RR.[26–38] Compared with metal oxides pre-catalysts, the residual nonmetal concentration of S, B, N and their influence on the metal oxidation state were different. Moreover, the different compositions of pre-catalysts can regulate the structure evolution and result in unique surface morphology and defects. Therefore, various $CO_2$RR selectivity and activity of pre-catalysts that superior to their pristine metal foil opponent have been realized, as listed in Table 1. For instance, Sargent group found that the nanostructure catalyst derived from Cu–F pre-catalysts can realize C2+ FEs of 85.8% at 1600 mA cm$^{-2}$.[31]

$Cu_2S$ catalysts with abundant vacancies on the surface were also created and exhibited faradaic efficiency for $C_3H_7OH$ and $C_2H_5OH$ of 8% and 15%.[26] Although there are numerous research works on the development of pre-catalysts, a practical rule or guideline for the design of pre-catalysts still lacks due to the difference in preparation methods, test methods, and sample parameters in each research work. There is an urgent need to sort out the relationship between the structure and performance of various pre-catalysts.

In this review, we systematically analyze the performance and structural evolution of pre-catalysts of metal oxides, metal dichalcogenide, metal nitrite, metal halogens and other metal salts. The composition or structural factors that strongly influence the $CO_2$RR performance are categorized into element residue, specific surface area increase, grain boundary, surface orientation, *etc.*, and the mechanism of their influence on performance is explained separately. The stability of the sample, especially the evolution of the element residue and the special surface structure under long-term operation is also analyzed based on the existing data. This article provides guidance on the relationship between structure and performance for future research in the field of pre-catalysts.

## 2. Pre-catalyst for $CO_2$RR: synthesis and characterization technique

With the in-depth characterization of catalysts based on various advanced techniques, it is widely accepted that most of the catalysts experienced a dynamic structural change during the reaction.[4,39,40] Thus, the real active sites and the finial composition/structure of the catalysts should be carefully determined. One example is the development of "bi-functional catalysts" for electrochemical water splitting. The as-synthesized metal borides, phosphides, nitrides, sulfides and selenides have been found to exhibit superior activity both for OER and HER.[4,39] However, a detailed investigation on these catalysts revealed that a structural/composition change is almost inevitable after a long-term operation. For OER, the as-prepared compounds tend to change to metal oxide/(oxy) hydroxide through the oxidation of the parent catalysts, which is driven by the thermodynamically potential according to the $E$–pH diagram. Similarly, metal phase is proposed to be the main composition of the derived catalysts after HER. The structural, morphological and chemical state changes during other catalytic processes such as $CO_2$RR, NO oxidation, CO oxidation, oxygen reduction *etc.* are also significant due to the applied potential and complex reaction environment.[40] The development of various advanced characterization techniques allows researchers to gain more in-depth insight into the catalyst change under electrochemical conditions.[40–42] Another issue should be considered is the unintentional introduction of impurities in derived catalysts. For example, Fe impurities are easy to be incorporated in the OER electrocatalyst during the synthesis and/or OER process, leading to the controversial conclusions and incorrect performance merits collected by different groups.[4] By carefully eliminate the Fe interference

This journal is © The Royal Society of Chemistry 2021

*J. Mater. Chem. A*, 2021, **9**, 19508–19533 | **19509**

**Table 1** The product distribution of selected pre-catalysts for $CO_2RR$

| Catalysts | Identified reason (besides high surface area) | Potential vs. RHE | $j_{total}$ (mA cm$^{-2}$) | Selectivity | | Ref. |
|---|---|---|---|---|---|---|
| | | | | Key products | Faradaic efficiency (%) | |
| $AuO_x$ | Grain boundaries | −0.4 | 6–10 | CO | 98% | 18 |
| AuOH | Grain boundaries | −0.59 | 2.6 | CO | 98% | 62 |
| $AuO_x$ | Surface disorder | −0.8 | 10–16 | CO | >90% | 61 |
| Au-complex | S anions | −0.68 | 4.4 | CO | 94.2% | 214 |
| $AgO_x$ | Nanostructured surface | −0.8 | 1.15 | CO | 89% | 20 |
| $AgO_x$ | Undercoordinated sites | −0.6 | 2.5 | CO | 90% | 108 |
| $AgO_x$ | Surface orientation | −0.6 | 3.7 | CO | 92.8% | 64 |
| $AgCl_x$ | Cl anions | −0.5 | 2 | CO | 95% | 32 |
| $AgI_x$ | I anions | −0.7 | 16.7 | CO | 94.5% | 107 |
| $AgP_2$ | Partially oxidized Ag | −0.8 | 9 | CO | 82% | 35 |
| Ag-complex | High surface area | −1.03 | 6 | CO | 96% | 182 |
| $Ag_2CO_3$ | Nanostructured surface | −0.55 | 1 | CO | 90% | 67 |
| $Ag_3PO_4$ | Nanostructured surface | −0.9 | 8 | CO | 93% | 156 |
| $GaO_x$ | Small metal particle | −0.71 | 5 | CO | 77% | 51 |
| CdS | Partial S coordination | −1.2 | 12 | CO | 95% | 81 |
| ZnO | Nanostructure | −0.85 | 10 | CO | 95% | 98 |
| ZnO | $Zn^{2+}$ rich surface | −0.95 | 7 | CO | 95.3% | 116 |
| $SnO_2$ | Grain boundaries | −0.8 | 6 | HCOOH | 80% | 109 |
| $SnO_2$ | Grain boundaries | −0.99 | 7 | HCOOH | 63% | 167 |
| $SnO_2$ | Small metal particles | −1.1 | 16 | HCOOH | 84% | 90 |
| $SnS_2$ | Residual S anions | −0.8 | 13.9 | HCOOH | 84.5% | 84 |
| $Bi_2O_3$ | Surface defects | −0.82 | 36 | HCOOH | >98% | 23 |
| $Bi_2O_3$ | Residual O anions | −0.9 | 8 | HCOOH | 91% | 25 |
| $Bi_2S_3$ | Surface defects | −0.75 | 5 | HCOOH | 84% | 25 |
| BiOCl | Shortened interlayer bond | −1.16 | 60 | HCOOH | 95% | 33 |
| BiOBr | Surface orientation | −0.9 | 55 | HCOOH | 95% | 152 |
| BiOI | Partial oxidized Bi | −1.0 | 40 | HCOOH | 90% | 222 |
| Bi-MOF | 2D nanostructure | −0.9 | 26.5 | HCOOH | 98.6% | 223 |
| Bi-MOF | Small metal particles | −0.97 | 5.4 | HCOOH | 95% | 155 |
| $Bi_2O_2CO_3$ | 2D nanostructure/subcarbonate | −0.7 | 11 | HCOOH | 85% | 68 |
| $Bi_2O_2CO_3$ | 2D nanostructure | −0.8 | 5 | HCOOH | 94% | 82 |
| $Cu_2O$ | Grain boundaries | −0.5 | 2.7 | CO | 40% | 16 |
| $Cu_2O$ | Higher $Cu^+$ coverage | −1.6 | 6 | C2+ | 59% | 140 |
| | | | | $C_3H_7OH$ | 8.7% | |
| $Cu_2O$ | Higher $Cu^+$ coverage | −0.9 | 20 | $C_2H_4$ | 60% | 110 |
| Regenerated $CuO_x$ | Higher $Cu^+$ coverage | −1.0 | 5 | C2+ | 76% | 24 |
| | | | | $CH_3CH_2OH$ | 32% | |
| $CuO_x$ | Nanostructure | −0.7 | 5 | $C_2H_6$ | 37% | 165 |
| $CuO_x$ | Residual O anions | −1.0 | 35 | $C_2H_4$ | 45% | 157 |
| | | | | $CH_3CH_2OH$ | 22% | |
| $CuS_x$ | S anions | −0.8 | 10.7 | HCOOH | 74% | 104 |
| $CuS_x$ | S anions | −0.95 | 32 | C2+ | 51% | 26 |
| | | | | $C_3H_7OH$ | 8% | |
| Cu(OH)Cl | Higher $Cu^+$ coverage | −1.2 | 22.2 | C2+ | 68% | 30 |
| | | | | $C_2H_4$ | 38% | |
| Cu(OH)F | F anions | −0.54 | 800(flow cell) | C2+ | 84% | 31 |
| | | | | $C_2H_4$ | 60% | |
| $CuI_x$ | Nanostructure | −0.735 | 20 | C2+ | 57.2% | 106 |
| | | | | $C_2H_6$ | 30% | |
| $Cu_3N$ | Higher $Cu^+$ coverage | −0.95 | 22 | C2+ | 64% | 224 |
| $Cu_3N$ | Nanostructure | −1.0 | 18.5 | C2+ | 68% | 55 |
| Cu(B) | Higher $Cu^+$ coverage | −1.1 | 70 | $C_2H_4$ | 52% | 38 |
| | | | | $C_2H_5OH$ | 27% | |
| Cu(B) | Nanostructure | −1.1 | 18.2 | $C_2H_4$ | 58.4% | 95 |
| Cu-MOF | Undercoordinated sites | −1.07 | 263(flow cell) | $C_2H_4$ | 45% | 36 |
| Cu-MOF | Higher $Cu^+$ coverage | −0.4 | 14 | $CH_3COO-$ | 48% | 153 |
| | | | | $CH_3CH_2OH$ | 32% | |

during synthesis and measurement, the role of Fe is elucidated and the real OER activity trends for certain catalysts can be reconstructed.[43–45] These results implied that the important role of determining the real active site of $CO_2RR$ catalysts by monitoring the structural evolution and the unintentional impurities. Thus, this section summarized the synthesis method for

**19510** | J. Mater. Chem. A, 2021, **9**, 19508–19533

This journal is © The Royal Society of Chemistry 2021

CO$_2$RR pre-catalyst and highlighted the specific function of various advanced characterization techniques, which is quite important for tackling the key challenges of the catalysts.

There are many effective ways to control and create the pre-catalysts from metal or metal salts precursors. Thermal treatment is one of the easiest ways to create metal oxides by placing the precursor in a muffle or tube furnace in an air atmosphere at the specified temperature and time period.[16,25,46–53] By using this method, the adventive element contaminations can be largely avoided as long as high-purity metal foil or precursor is used. Generally, several μm of copper oxide layer can be formed on copper foil after annealing at 500 °C for 12 h.[16,48] SnO with thickness ranging from 5.4 to 16 nm can be realized from Sn nanoparticle by changing annealing temperature between 100–180 °C and annealing period between 6–18 h.[52] PbO, Bi$_2$O$_3$, In$_2$O$_3$ and Ga$_2$O$_3$ can also be synthesized directly from Pb and Bi metal or In(acac)$_3$ and gallium nitrate precursor.[25,49–51] The thermal annealing method can also be applied to the synthesis of copper nitride pre-catalysts by the nitridation process of copper-based precursor under NH$_3$ flow with heating. Besides planar copper nitride, nanostructured copper nitride could also be realized by using CuO$_x$ with desired nanostructure as nitridation precursor.[54,55] Worth noting that thermal annealing method is not suitable to create thick oxide layer on Au and Ag metal. Au metal is difficult to be oxidized due to the high work function of 5.1 eV. Although Au$_2$O$_3$ has been observed as the oxidized state of Au, it is merely a metastable state at room temperature and will quickly decompose at $T > 160$ °C.[56,57] The thermal oxidation of Ag foils is also not effective because the instability of silver oxide at temperatures above 200 °C.[58] A mixture of metallic Ag (Ag(0)) and oxidized Ag was obtained after air annealing due to thermal instability of AgO$_x$ to Ag.[59,60]

Electrochemical oxidation at a highly positive voltage, on the other hand, can effectively oxidize Au(0) to Au(OH)$_3$ or Au$_2$O$_3$, and oxidize Ag(0) to AgO or Ag$_2$O, depending on the electrolyte identity and applied potential.[18,20,61–63] For instance, Kanan and coworkers applied a periodic symmetric square-wave potential routine at 1 kHz in 0.5 M H$_2$SO$_4$ for 60 min on a piece of Au foil, resulting in the formation of thick (>1 μm) and amorphous Au oxide layers.[18] Changing the electrolyte to neutral would result in Au(OH)$_3$ as products of anodization.[62] The potential anodization of Ag to AgO$_x$ was usually performed under a more alkaline solution, as Ma et al. reported the fabrication of Ag$_2$O layers by applying symmetric 50 Hz square-wave pulsed potential on polycrystalline Ag foil in 0.2 M NaOH solutions.[20] Zhou et al. reported that Ag started to get oxidized to form Ag$_2$O in neutral electrolyte when the potential was increased to 0.6 V, and was further oxidized to AgO at higher potential,[64] however, in an electrolyte with pH of 3, the anodization of Ag cannot form Ag oxides. Electrochemical oxidation is also a facile and common way to create nanostructured metal oxides. Cu$_2$O layer with nanowire morphology can be formed by anodization of a Cu layer in 3 M KOH.[65] Electrochemical oxidation by linear sweep voltammetry with high positive potential limits is also feasible to synthesize cubic Bi$_2$O$_3$ phase.[66]

The electrochemical oxidation method can also introduce other nonmetal element into metal lattice by anodic treatment in electrolyte with corresponding anions. For instance, an anodic potential of 2.6 V was reported to synthesize 4.9 μm Ag$_2$CO$_3$ layer on Ag foil in 3 min (ref. 67) and a direct current potential difference of 10 V was applied to synthesize white solid powder of Bi$_2$O$_2$CO$_3$.[68] Ag halide and CuS can be fabricated by electrochemical anodic treatment in corresponding halide and thiourea contained electrolyte, respectively,[32,69–71] while copper halides compounds can even be formed on the surface of Cu during CO$_2$RR in halide salts electrolytes.[72–74] Solvothermal synthesis is a very common and facile method to synthesize various of metal compounds and one of its prominent features is to create nanostructure morphologies.[23,26,30,31,34,75–88] Liu et al. reported the synthesis of ultrathin sub-2 nm SnO$_2$ quantum wires from SnCl$_4$ and oleylamine precursor.[89] A two-step strategy was developed to first synthesize Sn compound with controllable morphology, such as SnS$_2$ nanosheet, and then converted the Sn compound to SnO$_x$ by annealing.[90,91] In the work of Sun and coworkers, by raising the reaction temperature from 230 to 260 °C, the morphology of the final copper nitride products from solvothermal synthesis changed from nanoparticle to nanocube and then from 25 nm nanocube to 10 nm nanocube.[79] Hollow nanotubes composed of SnS (stannous sulfide) nanosheets was synthesized by the employment of MoO$_3$ template in solvothermal process.[27] Solvothermal methods were also developed to synthesize ZnO, B–CuO, bismuth sulphide, AgBiS$_2$, Ag$_2$S, InS and CdS, and nanostructure such as nanoneedles, nanorods, and nanoparticles can be realized.[28,29,80,81,92–98]

There are also other methods that can create metal compound pre-catalysts. For instance, since Cu is vulnerable to oxidation, chemical oxidation can be applied to form Cu(OH)$_2$ nanotube/nanowire/microflower by oxidant of (Na$_2$S$_2$O$_8$/K$_2$S$_2$O$_8$),[99–103] and even immersing Cu foil in ammonium poly-sulfide solution for 5 min can result in the formation of copper sulfide.[104] The direct reaction between metal foil and solution are further employed to fabricate Bi$_2$O$_2$CO$_3$, Cu-halide and Ag halide.[105–107] Plasma treatments can create metal oxides layer on metal and even control the nanostructure morphology and surface roughness of Cu, Ag and Sn pre-catalysts.[108–111] Electrochemical deposition is another common method to achieve metal oxides and was reported to fabricate Cu$_2$O,[75,112–114] SnO$_x$,[22] Cd(OH)$_2$ nanosheets[115] and ZnO[98,116] with structure parameters can be controlled by pH value, precursor concentration and deposition temperature. Compared with the high-cost vacuum deposition methods (e.g., ion-beam sputtering, magnetron sputtering, thermal evaporation), solution-based synthesis methods are the most popular means to fabricate CO$_2$RR catalysts with controlled morphology and nanostructures. However, it should be noted that the solution method is prone to introduce impurities in catalysts during synthesis and an intentionally purified process for the electrolyte is suggested to avoid contamination.

For the characterization techniques, normal X-ray diffraction (XRD), X-ray photoelectron spectroscopy (XPS), Scanning electron microscope (SEM), Transmission electron microscope (TEM), Atomic force microscope (AFM), have all been applied to measure the atomic and electronic structure of pre-catalysts and
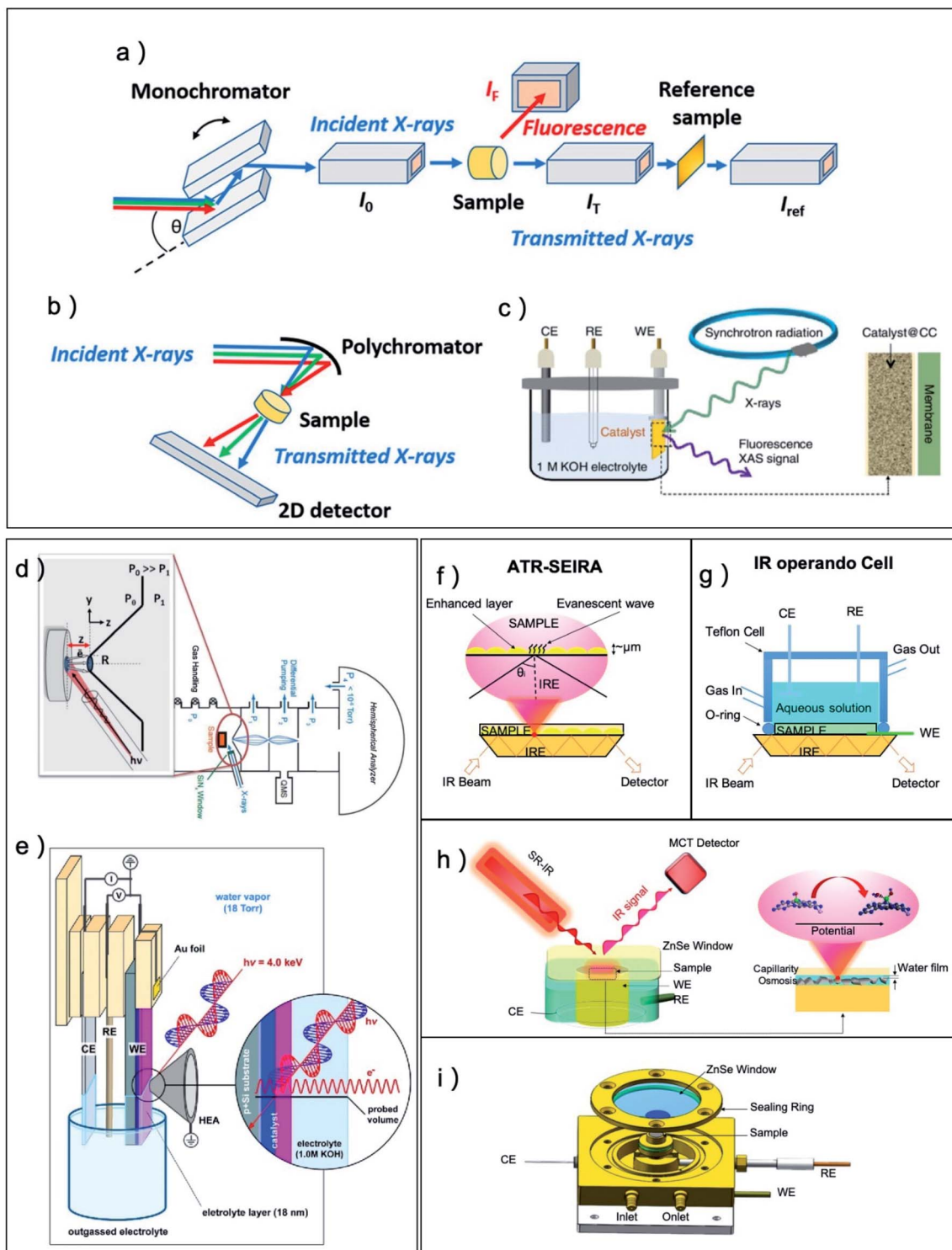
This journal is © The Royal Society of Chemistry 2021

*J. Mater. Chem. A*, 2021, **9**, 19508–19533 | **19511**

Fig. 1 (a–c) Typical configurations for electrochemical *operando* XAFS. (a) Schematics of a common setup XAS measurements with mono-chromator front end. (b) Schematics of XAS measurement with energy-dispersive mode. (c) A typical *operando* electrochemical cell set-up for electrocatalysis. CE, counterelectrode; WE, working electrode; RE, reference electrode. (d and e) Typical configurations for electrochemical *operando* APXPS. (a and b) Adapted with permission from ref. 42 Copyright © 2021, American Chemical Society. (c) Adapted with permission from ref. 122 Copyright © 2019, Springer Nature. (d) A typical APXPS setup used in ALS endstation. (e) Schematic illustration of the reaction cell configuration used for *operando* electrochemical APXPS. The electrode is pulled out of the electrolyte and covered by micron meters of aqueous solution. (d) Adapted with permission from ref. 120 Copyright © 2013, Elsevier. (e) Adapted with permission from ref. 121 Copyright © 2017, American Chemical Society. (f) Schematic representations of attenuated-total-reflection surface-enhanced infrared absorption (ATR-SEIRA). (g) Schematic illustrations of *operando* ATR-IR cells for electrocatalytic reactions. Schematic illustrations of (h) *operando* SRIR methodology and (i) *operando* SRIR cell. (f–i) Adapted with permission from ref. 5 Copyright © 2020, Elsevier.

19512 | *J. Mater. Chem. A*, 2021, 9, 19508–19533

This journal is © The Royal Society of Chemistry 2021

derived catalysts, however, to fully understand the real structure of catalysts during $CO_2RR$, numerous advanced *operando* methods have been adopted to the $CO_2RR$ system. To examine the structural and morphological change of catalysts under catalytic process, *in situ* and *operando* SEM, AFM and TEM operated under a liquid or gas-phase condition was developed to monitor the dynamic transformations.[40–42] Ambient pressure X-ray photoelectron spectrum (APXPS) can provide the electric structure information of catalysts surface for electrochemical $CO_2RR$ and the system is typically performed with electrochemical treatment and XPS in the same measurement chamber with ~10 Torr of water vapor.[117–121] After the electrochemical treatment, working electrodes were pulled out of the electrolyte into the XPS measurement position that was approximately several hundreds µm away from the analyzer entrance nozzle (Fig. 1d and e).

X-ray absorption fine structure (XAFS) is a very powerful method for the *operando* measurement of electrochemical reaction because both incident light and outgoing light are X-ray and have a high transmission depth in water (Fig. 1a–c).[42,122] XAFS are very sensitive to the local atomic and electric structure of element species in the catalysts from extended X-ray absorption fine structure and X-ray absorption near edge structure, and it can provide valuable information of catalytic metal centers for even amorphous sample. However, the XAFS method also has a high transmission depth in the sample and usually obtains the structure information of the whole bulk material. For $CO_2RR$ research, the incident mode is usually adopted to limit the detection at the surface layer.[21,110] *Operando* Raman is another method to probe the crystal structure evolution of pre-catalysts and is robust against the absorption of water.[123] The *operando* Raman configuration is based on reflective mode which is similar to that of the normal IR that measures sample in an aqueous solution. To amplify the signal of sample, plasmonic substrate such as nanostructured Ag, Au, and Cu are usually utilized to enhance the electromagnetic field at electrode surface and multiply the resultant Raman signal by several orders of magnitude. Fortunately, Ag, Au, and Cu are the most common metal catalysts studied for $CO_2RR$, which greatly simplify the design of surface-enhanced Raman spectroscopy in this area. Using surface-enhanced Raman spectroscopy, Han and coworkers successfully probed the difference of intermediate species on four commonly used Cu catalysts,[124] and they also discovered that the CO adsorption configuration on Cu is different when changing the pH value of the electrolyte.[125] For other metal catalysts that are non-plasmonic or with flat surface, a newly emerging technology of shell-isolated nanoparticle enhanced Raman spectroscopy (SHINERS) exhibit great potential to enable the amplification of Raman signal.[124,126] In this method, plasmonic nanoparticles, which are enclosed within a shell composed of an insulating material, are placed in close proximity with a non-plasmonic catalyst to impart a similarly increased electromagnetic field to the material of interest.

The *operando* IR, on the other hand, can provide strong signal for polar groups such as C–O, O–H and C–H on the surface of the catalyst and helps to understand the reaction pathway of $CO_2RR$ on catalysts with different selectivity.[5,71,127,128]

The *operando* IR is very vulnerable to the absorption of water and usually adopts total reflection mode and the pre-catalyst sample is deposited on the surface of internal reflective element (Fig. 1f and g). The electromagnetic field of this reflected IR beam at the boundary can still extend into the sample medium and obtain the information of functional groups on the surface of the sample.[5] Notably, when utilizing the synchrotron radiation (SR) light source with high brightness at a microzone, even external reflection mode IR technology can obtain sufficient signals of surface bonding groups, which can greatly simplify the experimental design for dilute catalytic site systems (Fig. 1h and i). The rational design of pre-catalysts for enhanced activity, selectivity and stability demands precise controlling of the initial composition, chemical state and nanostructure in the synthesis process. Meanwhile, the structural/chemical parameters of the catalysts should be carefully monitored under realistic operation conditions due to the pre-catalysts actively transform and sensitively respond to the electrochemical reaction environment. Thus, tremendous efforts have been conducted to correlate dynamic parameters change of the pre-catalysts to the activity trend that aims to reveal the nature of active sites in the derived catalysts.

# 3. The role of residual anion ions in metal–nonmetal compound derived catalysts during $CO_2RR$

## 3.1. The existence of anion ions in derived catalysts

### 3.1.1 The existence of O in metal oxide derived catalysts.
Many well-known metal catalysts, such as $CuO_x$, $AuO_x$, $AgO_x$, $SnO_x$ and $ZnO_x$ have been studied as $CO_2RR$ pre-catalysts. Theoretically, a phase diagram of these metal/metal-oxides in an electrochemical aqueous environment can be calculated by the equilibrium of redox and acid–base reactions as shown in Fig. 2.[123,129–134] It is obviously that the standard electrode potential (SEP) of most of these $M/Mn^+$ (M: metal) are positive or close to 0 *vs.* RHE and the stablest phase of the pre-catalysts are pure metal at the $CO_2RR$ potential that more negative than 0 V *vs.* RHE according to the Pourbaix diagram (in this paper all voltages used are *vs.* RHE, unless specially noted such as the case in Fig. 2). However, the electrochemical reduction of metal oxides may not fully complete because of the competition reaction or not exposing to the electrochemical active interface. It is crucial to find out the concentration and local structure of oxygen in $MO_x$ under $CO_2RR$ reaction to understand the real role of $MO_x$ pre-catalysts.

There are two main obstacles to find out what is the real state of oxygen in $MO_x$ pre-catalysts under $CO_2RR$. First, the remnant concentration of O might be too low to be detected by bulk methods such as normal XRD.[20,21] Second, the surface of some metal, such as Cu, are very sensitive and vulnerable to the oxidation of air. Thus, the clear signal of oxygen observed in XPS measurement may not really correspond to the remnant of oxygen on the catalyst surface.[16,135,136] For instance, Lum *et al.* reported that there is no $Cu_2O$ signal for OD-Cu under $CO_2RR$, however, once the potential was removed, $Cu_2O$ peaks began to
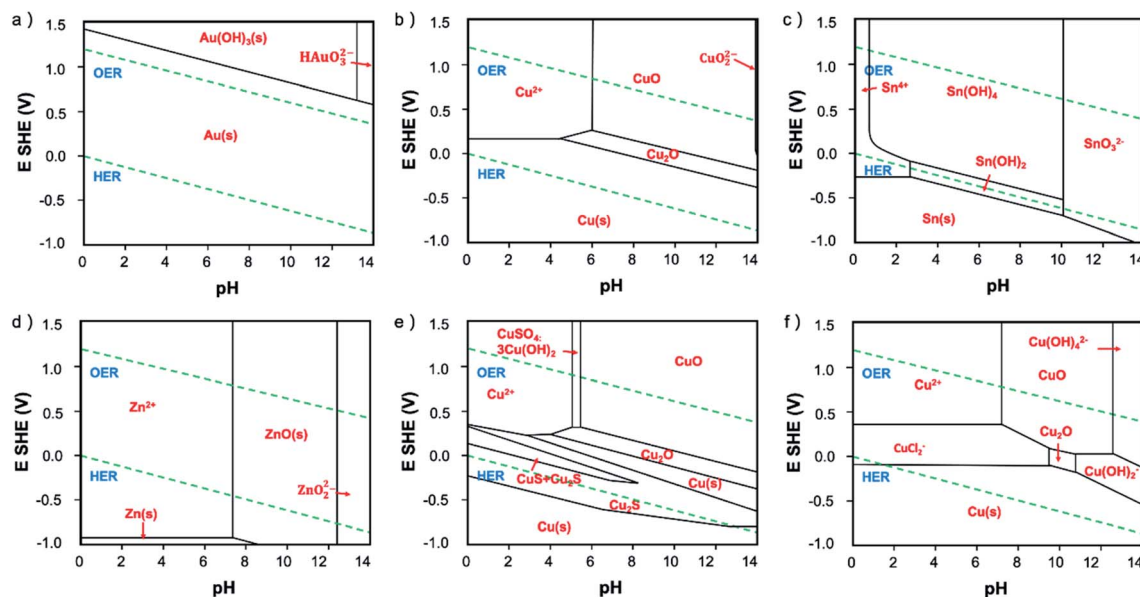
This journal is © The Royal Society of Chemistry 2021

*J. Mater. Chem. A*, 2021, **9**, 19508–19533 | **19513**

**Fig. 2** The Pourbaix diagram of (a) Au–H₂O, (b) Cu–H₂O, (c) Sn–H₂O, (d) Zn–H₂O, (e) Cu–S–H₂O and (f) Cu–Cl–H₂O at 25 °C. Au, Cu, Sn and Zn Pourbaix diagram are produced with a total concentration of $[M(aq)]_{tot} = 10^{-4}$ M. Cu–Cl–H₂O Pourbaix diagram is produced with total concentration of $[Cu(aq)]_{tot} = 10^{-6}$ M, and $[Cl(aq)]_{tot} = 0.2$ M. Cu–S–H₂O Pourbaix diagram is produced with total concentration of $[Cu(aq)]_{tot} = 0.001$ M and $[S(aq)]_{tot} = 0.0009$ M.

appear again after 60 s.[137] To this end, *in situ* detection techniques and high-sensitive surface methods are required to further investigate the real composition of the catalyst surface and its influence on CO₂RR.

The most common *in situ* method to detect the oxygen in MO$_x$ is APXPS, which can provide clear signal for oxygen on surface or subsurface of catalysts.[118] The quasi *in situ* oxygen K-edge electron energy-loss spectra (EELS)[118] is also a powerful method to determine the state of O on surface. *In situ* X-ray absorption fine structure and near edge structure (XAFS; XANES) have a much higher investigation depth, but they can be still employed to provide surface information by incident mode.[21,110] The results showed that the residual O in metal oxides under CO₂RR is still strongly related to the SEP of M/M$^{n+}$. For metal with very positive SEP, such as Au (SEP: 1.002 V, all SEP are *vs.* RHE) and Ag (SEP: 0.7996 V), there is no signal of AuO$_x$ or AgO$_x$ in XRD after CO₂RR.[18,20] XPS and EDXS exhibited the expected peaks for Au(0) and no peaks related to an Au oxide can be found, indicating that reduction of Au₂O₃ was complete within the detection limits of these techniques.[18] However, the monitoring of surface AgO$_x$ structure by *operando* XAFS with grazing incidence mode (0.1° angle), as shown in Fig. 3a–c, clearly showed that a mixture of both metallic and oxide composition is maintained on the surface of OD-Ag.[21] The existence of stable O in OD-Ag was also confirmed by other methods such as Ag M$_{4,5}$VV Auger signals.[138] Cu is the metal that attracts the most attention in CO₂RR and has a much negative SEP (0.3419 V) compared with Ag. Based on *in situ* ambient pressure XPS, quasi *in situ* oxygen K-edge electron energy-loss spectra (EELS), positron annihilation spectroscopy (PAS) and *in situ* XANES, a clear signal of O has been observed in many OD-Cu electrocatalyst research and the O signal is found

to be relatively stable during CO₂RR.[118,139,140] This O signal is assumed to be subsurface oxygen in Cu lattice as no copper oxides can be observed in Cu 2p$_{3/2}$ APXPS spectra (Fig. 3d and e). However, there is no unified opinion on the oxygen content, existence shape and stabilization time of O in OD-Cu.[137] It is possible that the state of oxygen in OD-Cu is strongly related to the morphology of catalysts, electrolyte environment and reduction potential. Sn has a more negative SEP (−0.1375 V) compared with Cu; the concentration of O is much higher in OD-Sn and the phase of SnO$_x$ can be maintained during CO₂RR with low overpotential. The *operando* Raman spectroscopic survey performed by Broekmann and coworkers clearly exhibited that the practical (kinetic) stability region of SnO and SnO₂ well exceeds the thermodynamic stability window of Pourbaix diagram (hydrous Sn(ɪᴠ) oxide exist for $V > 0.1$ V; hydrous Sn(ɪɪ) oxide exist for $V = -0.1$–0.1 V; Fig. 2 and 4).[123]

There are also other metal oxides pre-catalysts, such as PbO$_x$ (SEP: −0.1262 V), InO$_x$ (SEP: −0.34 V), BiO$_x$ (SEP: 0.32 V), CdO$_x$ (SEP: −0.4030 V), GaO$_x$ (SEP: −0.549 V), ZnO$_x$ (SEP: −0.7618 V), however, the O state in these pre-catalysts have not been studied by *operando* surface detection methods. Based on the *ex situ* measurement or *in situ* bulk XAFS, the final phase of PbO$_x$, CdO$_x$, GaO$_x$ and BiO$_x$ after CO₂RR are mostly metal phase, however, the residual O in OD-metal can not be excluded.[23,49,51,115] Zn is the most active metal among these CO₂RR catalysts and a large amount of the oxygen can be maintained in the metal lattice even after CO₂RR.[116] In most research works, the final crystal phase of OD-Zn after CO₂RR is pure metal Zn,[97,98] however, Zeng and coworkers reported that ZnO phase could be maintained in ZnO nanosheets,[96] indicating that the stability of ZnO is strongly related to the sample morphology and experimental conditions.

**19514** | *J. Mater. Chem. A*, 2021, **9**, 19508–19533
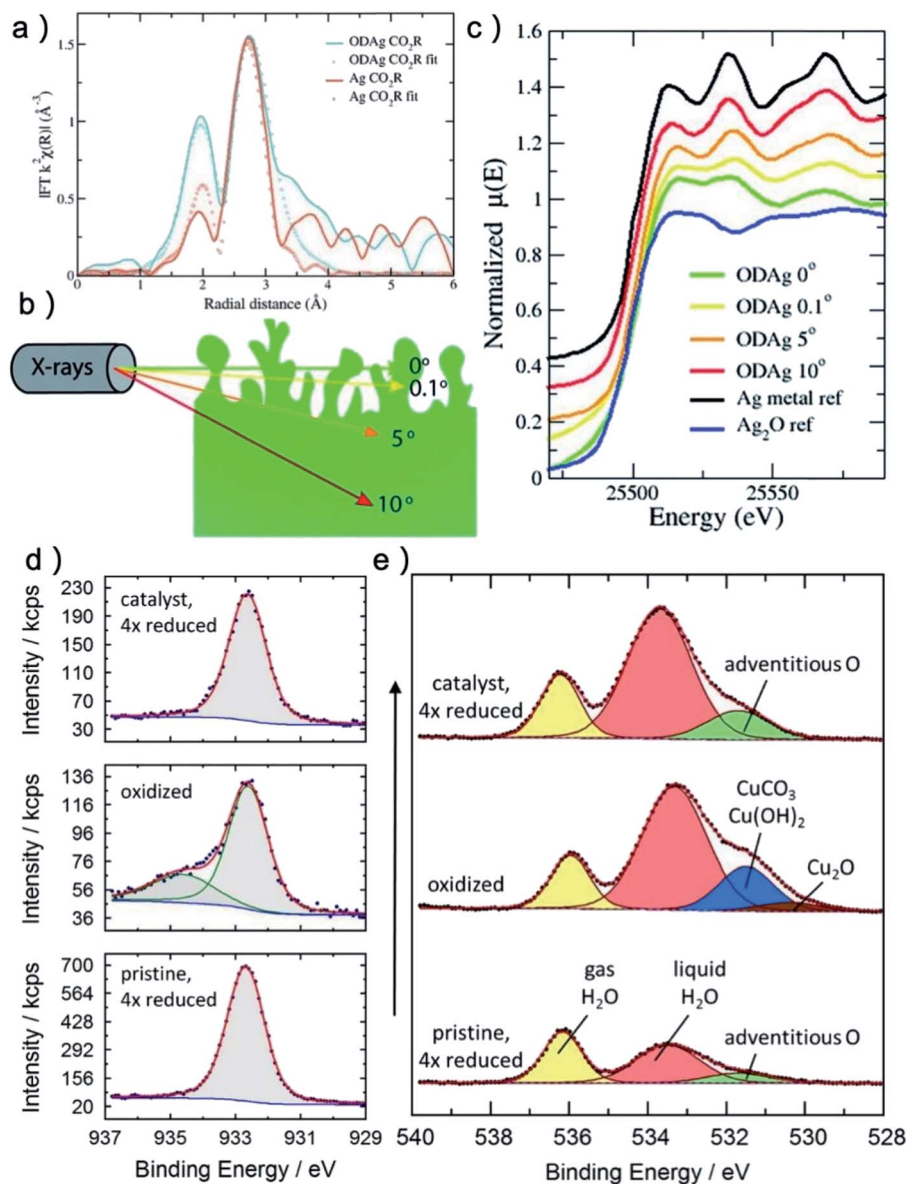
This journal is © The Royal Society of Chemistry 2021

Fig. 3 (a) $k^2$-Weighted Fourier transformed EXAFS fluorescence spectra of a Ag catalyst and an oxide-derived Ag catalyst. (b) Schematic illustrations of *operando* grazing incidence X-rays absorption measurement on OD-Ag. (c) *Ex situ* normalised XANES spectra of OD-Ag samples. With smaller incident angle, more Ag–O signal can be detected. (a–c) Adapted with permission from ref. 21 Copyright © 2019, Royal Society of Chemistry. (d) *In situ* Cu $2p_{3/2}$ APXPS spectra of oxidized and reduced sample. The oxidized spectrum shows an additional Cu(II) compound while the reduced sample shows no Cu(II). (e) *In situ* O 1s APXPS spectra of pristine sample, oxidized sample and reduced sample. The reduced sample contains significantly more adventitious oxygen (green) than the pristine sample before oxidation. (d and e) Adapted with permission from ref. 118 Copyright © 2019, American Chemical Society.

The state of oxygen in mixed metal oxides pre-catalysts are more complex because the interaction between metal atoms may stabilize the M–O bond in the pre-catalysts. For instance, the Cu ions in mixed metal oxide of $CuInO_2$ are found to be much more difficult to reduce than that in $Cu_2O$.[141] $Sn^{2+}$ ions were found to be stabilized by many binary structure, such as Bi–$SnO$,[142] Cu–$SnO_x$,[143] $SnO_x/AgO_x$,[144] which are probably due to the activity difference of these two metals that result in the rearranging of the free electrons.

**3.1.2 The existence of other nonmetal element in derived catalysts.** Besides the success of metals oxide pre-catalysts, the

progress of other metal–nonmetal pre-catalysts also attract great attention, such as metal dichalcogenides, metal halide, metal nitride, MOF and other metal salts.[26,29,31,33,34,68,77,145] It is easier to distinguish the remnant concentration of these nonmetal elements because the concentration of remnant nonmetal are not impacted by the re-oxidation of catalyst in air. Thus, the normal detection methods such as XRD and XPS can provide reliable information for the state of nonmetal elements after $CO_2RR$.

Generally, the stability of metal dichalcogenides under $CO_2RR$ is similar to metal oxides. After $CO_2RR$, the XRD

This journal is © The Royal Society of Chemistry 2021

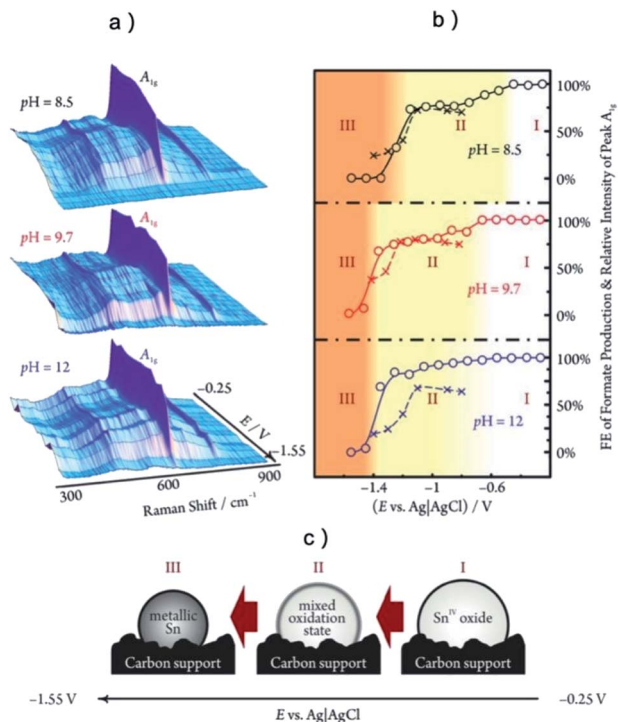J. Mater. Chem. A, 2021, **9**, 19508–19533 | **19515**

**Fig. 4** (a) The *operando* Raman studies of $SnO_2$ during $CO_2RR$ at different potential and pH. (b) The relative intensities of the Sn(IV)-related $A_{1g}$ Raman peaks (○, solid line) and the faradaic efficiencies of formate production (×, dashed line) as a function of electrode potential. (c) In region (I), $SnO_2$ remain fully oxidized; in region (II) the $SnO_2$ is partially reduced to SnO; in region (III) $SnO_2$ is fully reduced to metallic Sn. The highest selectivity for formate production existed in a potential range where the $SnO_2$ phase is metastable. (a–c) Adapted with permission from ref. 123 Copyright © 2015, American Chemical Society.

detection confirms the disappear of metal dichalcogenides phases for Cu, Au, Bi, Pb, Sn and Ag dichalcogenides pre-catalysts.[28,29,146] However, there is clear signal of S for CuS, $SnS_2$ and Ag–Bi–S pre-catalysts after $CO_2RR$ in XPS or energy-dispersive X-ray spectroscopy (EDS),[71,104,146] indicating that S may not be fully cleaved. For instance, Shao-horn and coworkers reported that for electrodeposited $Cu_xS$, only Cu metal and a tiny amount of $Cu_2O$ can be observed after $CO_2RR$, however, the S concentration is still one-tenth compared with the as-prepared $Cu_xS$,[71] as shown in Fig. 5a–c. As a result, the oxidation state of Cu in SD-Cu is much higher than that of the Cu foil. Worth noting that there are reports of $MoS_2$, $WS_2$, $MoSe_2$, $WSe_2$, $TiS_2$, ZnS and S-doped In as efficient $CO_2RR$ catalysts,[80,147–151] which did not exhibit large composition or morphology change during $CO_2RR$ and may be recognized as a new group of catalysts rather than pre-catalysts of metal. However, considering most of the metal–nonmetal catalysts are not really stable under $CO_2RR$ conditions, more research work on these catalysts is recommended to clarify the structural evolution behavior under high operation current (>500 mA $cm^{-2}$) and long operation time (>100 h). For example, the research of Cu–N, Cu–B and Ag–P pre-catalysts revealed that they were also vulnerable to $CO_2RR$,[34,35,95]

however, the concentration of N, B and P are much higher compared with O in Cu–O and Ag–O after long-term operation.

The halide of Cu, Ag and Bi were generally converted to pure metal phase under $CO_2RR$ based on XRD, while clear signal of halide on the surface of reduced catalysts can be observed in XPS or EDX.[31,32,69,107,152] For instance, Cu-halide pre-catalysts of Cu(OH)F synthesized by solvothermal method[31] exhibited initial surface halogen contents of 6 mol% which remained unchanged at ∼6 mol% in the first hour and decreased progressively to ∼4 mol% after 40 h. The high stability of surface halogen ions is because of the strong bonding of halogen to the electrode surface. In Polyansky's study,[32] the bonding between surface $Cl^-$ species and the Ag surface atoms is very strong with a high desorption temperature of 700 K. Li and coworkers observed the formation of cuprous halides with well-controlled tetrahedral shapes by simply immersing Cu foil in the aqueous solution of corresponding halide salts (NaCl, KBr, or KI) for 5 min.[106]

The research works for other metal–nonmetal pre-catalysts, such as MOF, metal salts, V group element compound, are much less compared with the aforementioned categories and mostly focused on Cu, Ag and Bi based pre-catalysts. Based on the limited data, the MOF of Cu, Ag and Bi are all unstable under $CO_2RR$,[36,153–155] resulting in the partially reduced MOF-derived catalysts and the formation of small metal clusters. Metal salts such as $Ag_3PO_4$, $Ag_2CO_3$ and $Bi_2O_2CO_3$ on the other hand, were observed to be fully reduced during $CO_2RR$ based on XRD and XPS.[67,82,156]

Based on these results, it is clear that the stability of nonmetal elements under $CO_2RR$ is related to SEP, bonding strength between cation and anion and the solubility of anion in the electrolyte. Although the leaching of anions from the parent catalysts into electrolytes is significant during $CO_2RR$, the residual anions still play an important role in affecting the electronic structure of the catalysts and determining the adsorption properties of intermediates. Thus, the role of anions existed in derived catalysts should be clarified to guide the design of highly efficient $CO_2RR$ catalysts.

### 3.2. The influence of residual anion ions on $CO_2RR$ activity

The pre-catalysts derived metal catalysts usually have various structural parameter changes, thus it is difficult to find direct evidence in the spectrum about the mechanism of how residual nonmetal element alone impact $CO_2RR$. However, an obvious relationship between the $CO_2RR$ activity of derived catalysts and the concentration of nonmetal element or $M^+$ ions have been observed, indicating that the existence of nonmetal element could raise the valence state of metal to impact the $CO_2RR$ performance. For instance, Gao *et al.* reported that Cu nanocube sample treated with $O_2$ plasmon maintain a much higher O content (30 at% *vs.* 14 at%) and C2+ faradaic efficiency (73% *vs.* 40%) compared with untreated Cu nanocubes.[157] KCl was also found to suppress the reduction of $Cu_2O$ and maintain a higher $Cu^+$ content compared with normally reduced $Cu_2O$,[140] resulting in an impressive 8.7% of FE $C_3H_7OH$. This phenomenon also held for Ag–O pre-catalysts as Smith group reported
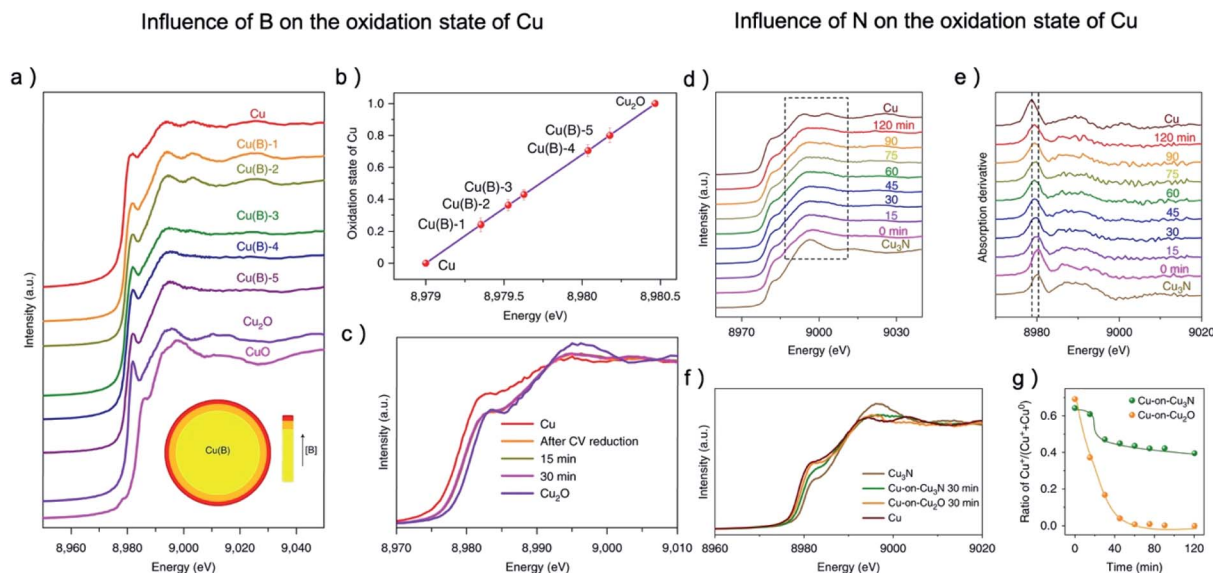
**19516** | *J. Mater. Chem. A*, 2021, **9**, 19508–19533

This journal is © The Royal Society of Chemistry 2021

**Fig. 5** (a) XRD, (b) Cu $2p_{3/2}$ XPS, (c) S 2p XPS of $Cu_xS$, SD-Cu and reference Cu foil. The sulfur XPS curve of $Cu_xS$ was reduced for 10-times for comparison. (d) Faradaic efficiencies for all detected products at different potential. (e) Partial current densities for hydrogen and formate. (a–e) Adapted with permission from ref. 71 Copyright © 2018, American Chemical Society.

that the faradaic efficiency for CO is proportional with the O/Ag ratio extracted by EXAFS fitting, while there is no clear relationship between $CO_2RR$ performance and surface area or Ag–O bonds numbers.[21] The situation for $SnO_x$ pre-catalysts is slightly different, because partial oxidized $SnO_x$ exhibited a better activity compared with both Sn and $SnO_2$, as shown in Fig. 4b.[22,52,123] Kanan group reported that catalyst with a $SnO_x$- : $Sn_0$ ratio of 93 : 7 showed the best HCOOH selectivity of 80%.[22]

The research of other metal–nonmetal pre-catalysts showed that many nonmetal elements can be more stable compared with O under $CO_2RR$ and can influence the $CO_2RR$ activity by raising the valence value of the metal center. Sargent and coworkers synthesized Cu(B) samples with porous dendritic morphology.[38] From XANES, the average oxidation state of copper is increased from 0.25 to 0.78 when the boron concentration increased from 1.3% to 2.2%, and the oxidation state is stable over the course of $CO_2RR$ (Fig. 6a–c). A volcano relationship between the oxidation state of copper and the FE of C2 products can be observed and the highest FE of 79% was achieved when Cu's valence value is +0.35, which is much higher than that of the pristine copper (29%) and OD-Cu (37%). The research of Cu–N also showed apparent residue of N after

$CO_2RR$ which greatly boost the C2 selectivity.[34,79] Especially, the investigation of Cu-on-$Cu_3N$ catalyst by *in situ* XAS found that the reducing of $Cu_3N$ was alleviated after the initial 60 min, while $Cu_2O$ was fully reduced after 1 h, as shown in Fig. 6d–g.[34] The stronger interaction between N and Cu on $Cu_3N$ pre-catalysts results in a 6.3-fold and 40-fold enhancement in the ratio of C2+/$CH_4$ compared to Cu-on-$Cu_2O$ and pure Cu catalysts, respectively. Specifically, the FE for $C_2H_4$, $C_2H_5OH$, and $C_3H_7OH$ are 39 ± 2%, 19 ± 1%, and 6 ± 1%, respectively, at −0.95 V.

The research of metal halide pre-catalysts further revealed that the electronegativity of the nonmetal element is crucial for the concentration of $Cu^+$ in the final derived catalyst. Sargent group synthesized Cu(OH)F, $Cu_2(OH)_3Cl$, $Cu_2(OH)_3Br$ and CuI by solvothermal method.[30,31] They found that the average oxidation states of copper in the X–Cu catalysts is proportional with the electronegativity of the halogen,[31] as shown in Fig. 7d. The results revealed that the onset potential of $C_2H_4$ decreases significantly with the increase of electronegativity of halide ions. The best performance was achieved over the F–Cu catalyst with C2+ FEs of 85.8% at 1600 mA $cm^{-2}$, as shown in Fig. 7e, and a large amount of surface-bound CHO species, a key intermediate for C–C coupling, can be observed on F–Cu

This journal is © The Royal Society of Chemistry 2021

*J. Mater. Chem. A*, 2021, **9**, 19508–19533 | **19517**

Influence of B on the oxidation state of Cu

Influence of N on the oxidation state of Cu

**Fig. 6** (a) The copper K-edge XANES spectra of Cu(B) samples after being electrochemically reduced, with CuO and $Cu_2O$ as reference. (b) The oxidation state of reduced Cu(B) samples calculated from copper K-edge XANES spectra, (c) the copper K-edge XANES spectra of Cu(B) samples after CV reduction, 15 min later and 30 min later in comparison to pristine copper and $Cu_2O$. (d) The copper K-edge XANES spectra and (e) their first derivatives of the Cu-on-$Cu_3N$ catalyst as function of reaction time at −0.95 V. The reducing of $Cu_3N$ was alleviated after the initial 60 min. (f) *In situ* Cu K-edge spectra during the initial 30 min on Cu-on-$Cu_3N$ and Cu-on-$Cu_2O$. (g) Ratio of $Cu^+$ relative to total Cu for Cu-on-$Cu_3N$ and Cu-on-$Cu_2O$ during $CO_2RR$ at −0.95 V. The reducing of $Cu_2O$ was much faster than that of $Cu_3N$. (a−c) Adapted with permission from ref. 38 Copyright © 2018, Springer Nature. (d−g) Adapted with permission from ref. 34 Copyright © 2019, Springer Nature.
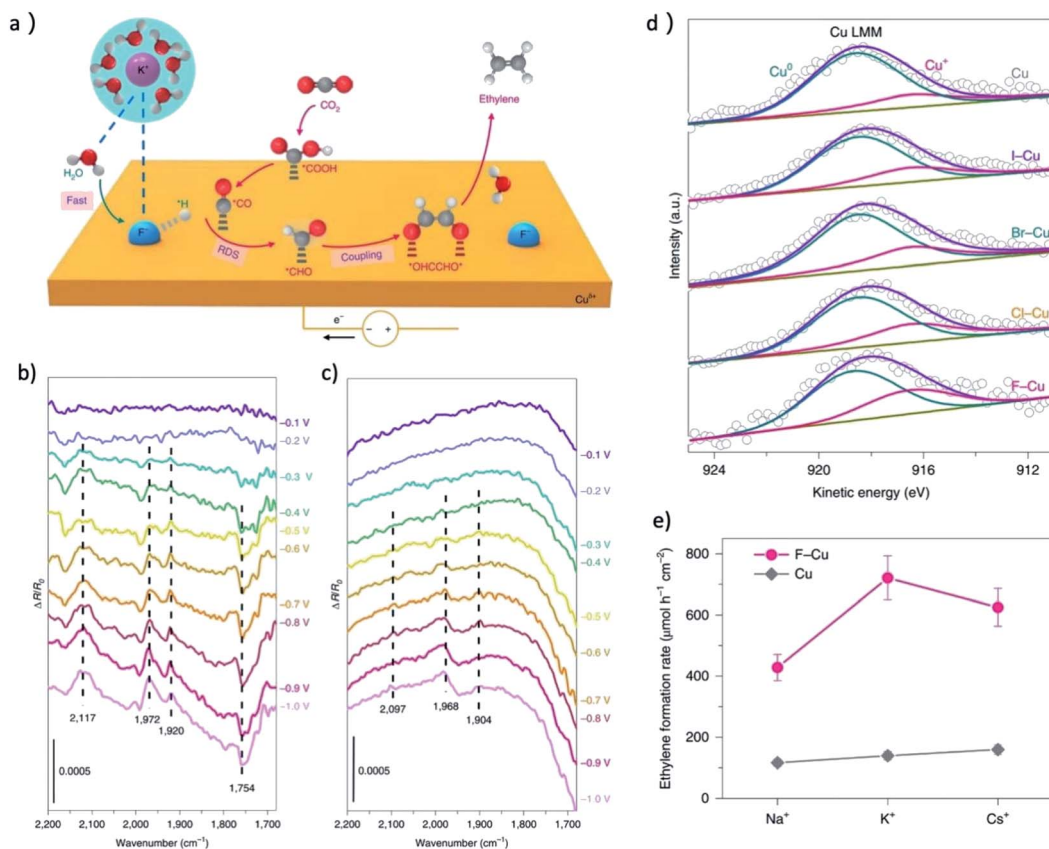
catalyst in comparison to normal copper by *in situ* ATR-FTIRS (Fig. 7b and c). Notably, the surface area normalized C2+ formation rates also increased in the sequence of Cu < I–Cu < Br–Cu < Cl–Cu < F–Cu, indicating this is an intrinsic difference of $CO_2RR$ activity.

The nature of how nonmetal residues influence the performance of metal catalysts is also studied by DFT calculations, which indeed show that the residual nonmetal can benefit the $CO_2RR$ on the derived catalyst. Most of the DFT calculations were focusing on the local structure of O in Cu catalysts and its influence on the $CO_2RR$ performance. Based on DFT calculations, albeit subsurface oxygen ($O_{sb}$) is not stable below the Cu surface in the slab model, it is stable below facets of a manually "reduced" Cu nanocube model, which is consistent with the experiment.[158] Such disordered structure increases the stability of subsurface oxygen in it. The presence of $O_{sb}$ enhances the adsorption energy of CO on Cu(100), and in turn increase the probability of CO dimerization, which is a rate-determining step toward the production of ethylene. Gu *et al.* reported the oxygen vacancy-rich $CuO_x$ surfaces can provide strong binding affinities to the intermediates of *CO and *COH, but weak affinity to *$CH_2$, thus leading to efficient formation of $C_2H_4$.[159] Other theoretical calculations claimed that the hydroxy group on the surface of OD-Cu would strongly influence the selectivity of $CO_2RR$.[160,161] Electronic structure analysis indicates that the charge transfer from hydroxy groups to coordination-unsaturated Cu sites stabilizes surface-adsorbed COOH*, which is a key intermediate during the $CO_2RR$. For other nonmetal elements such as B, F and S, DFT calculations also suggest that they are quite stable in the subsurface sites and

could introduce a strong impact on the adsorption of CO on metal.[31,38,146] Notably, Qiao and coworkers systematically calculated the Cu–X (X = B, N, P, S, Cl, Br, or I) catalysts and found that the electronegativity difference between the doping element and oxygen strongly impacted the O affinities of the dopant atom site and Cu site.[162] As a result, the ethane selectivity of all Cu–X catalysts were enhanced while the ethanol selectivity were generally suppressed. Cu–X catalysts doped with strong O affinity atoms, such as B, P, N, S, could favor the ethylene pathway due to the bonding between O and X. The influence of nonmetal element on the $CO_2RR$ catalytic activity of metal center can also be revealed by the study of metal–organic compound catalysts, which have a clear coordination structure of M–X. For instance, Strasser and coworkers studied metal- and nitrogen-doped porous carbons and discovered that the coordination environment of M–$N_x$ determined the binding energy of *H and *CO on metal center, which in turn decided the selectivity of $CO_2RR$.[163]

For most of the pre-catalysts, the final derived catalyst generally could suppress the hydrogen evolution, promote the selectivity of the major products and increase the current density, as shown in Table 1 for the $CO_2RR$ performance of typical pre-catalysts. However, the selectivity change of CuS is dramatically different compared with that of $CuO_x$ as many research works reported CuS have a strong trend to produce HCOOH.[71,78,104] In these reports, HCOOH accounted for more than 60% of the total FE and was the only carbon-based product (Fig. 5d and e). The SEIRAS result showed that there is a strong adsorbed CO layer on CuS, unlike in the Cu foil case,[71] which might block the $CO_2$-to-CO reaction pathway. DFT calculation

**19518** | *J. Mater. Chem. A*, 2021, **9**, 19508–19533

This journal is © The Royal Society of Chemistry 2021

Fig. 7 (a) A proposed reaction mechanism for the enhancement of $CO_2RR$ to $C_2H_4$ on F−Cu. Purple, potassium; blue, fluorine; red, oxygen; grey, carbon; white, hydrogen. (b) *In situ* ATR-FTIRS recorded at different applied potentials for the F−Cu catalyst in 0.1 M $KHCO_3$ electrolyte. (c) *In situ* ATR-FTIRS recorded at different applied potentials for the copper catalyst in 0.1 M $KHCO_3$ electrolyte. The band at around 1754 $cm^{-1}$ could be ascribed to the surface-bound CHO species, a key intermediate for C−C coupling. (d) Copper LMM Auger spectra of the X−Cu catalysts. The concentration of $Cu^+$ was observed to increase with with the electronegativity of the halogen. (e) The formation rate of $CO_2RR$ to $C_2H_4$ at −0.6 V over F−Cu and Cu in different electrolyte. Adapted with permission from ref. 31 Copyright © 2020, Springer Nature.

further confirmed that additive S would result in strong CO* adsorption and enhance the CO* coverage up to nearly 4 times higher than on a clean Cu surface.[164] A synergistic effect between residual S and CO* is the reason for the blocking of other reaction pathways except for HCOOH production. Although a series of research provide repeatable results that CuS pre-catalysts can only produce HCOOH, Sargent group reported that a $Cu_2S$ catalyst with abundant vacancies on the surface had faradaic efficiency for $C_3H_7OH$ and $C_2H_5OH$ of 8% and 15%,[26] indicating that more research is needed to understand the unique situation of Cu–S pre-catalysts.

## 4. The enhancement of surface area on derived catalysts

The oxidation–reduction process of pre-catalysts was reported to enhance the surface area of final metal catalysts compared with untreated metal catalysts. This can be attributed to the reconstruction of catalyst surface and the release of anions during the reduction of $M^+$ to M that leads to the formation of vacancies in the lattice. Compared with the initial planar metal film or untreated metal nanoparticles, several to several hundred

times improvements in electrochemically active surface area (ECSA) can be achieved on derived catalysts after $CO_2RR$.[16,28,46–48,54,55,66–68,83,87,90,91,99,105,110,155,156,165–169] For instance, in Kanan's report, the surface area of OD-Cu that prepared by thermal annealing and electrochemical reduction is 480 times higher than that of a polycrystalline Cu.[16] The partial reduction of $SnO_2$ lead to the formation of small Sn nanoparticles on the surface of nanostructured $SnO_2$, resulting in a large surface area of the porous nanosheet $SnO_x$ of 93.6 $m^2$ $g^{-1}$.[90,91] However, in most of the research works of pre-catalysts, the improvement of $CO_2RR$ performance can not be explained by the increase of surface area alone due to the significant enhancement of $CO_2RR$ at low overpotential and the suppression of hydrogen evolution. For OD-Au reported by Kanan, the roughness factor of 72 can be realized for the resulted agglomerated Au NPs with particle sizes of ∼20–40 nm, which is significantly smaller than the differences in $CO_2RR$ current density over the course of electrolysis (500 times difference at −0.4 V).[18] Zhou and coworkers showed that the OD-Ag leads to a 5 times larger ECSA enhancement but 21 times increase of $CO_2RR$ current density at 0.5 V overpotential compared to pristine Ag.[64] The situation is more complex for Cu based pre-catalysts because in many

This journal is © The Royal Society of Chemistry 2021

*J. Mater. Chem. A*, 2021, **9**, 19508–19533 | **19519**

reports the normalized current of $CO_2RR$ using ECSA is even less for OD-Cu compared with un-oxidized copper foil,[165,170] an optimal roughness and ECSA exists for $CO_2RR$ performance indicating that roughness is not the only reason for improved $CO_2RR$.[48,114,165]

One explanation of selectivity and activity enhancement at low overpotential for high roughness catalysts is that they have a strong impact on the solution environment near the electrode surface. The high surface area can benefit the catalytic current at low overpotential but hinder the replenish of consumed proton and $CO_2$ from bulk solution. The high local pH environment could greatly suppress the HER and favor $CO_2RR$. This pH-induced performance improvement is evidenced by increasing the thickness of the porous Au or Ag film, resulting in a 10–30 times increase of $CO_2RR$/HER ratio and >90% CO selectivity.[171–173] A finite element numerical model was also applied to establish an accurate 3D geometrical representation of an ordered meso-structured Ag electrode and revealed that roughness factor is crucial to determine the electrolyte composition and pH value near catalyst surface.[174] A substantial build-up of $OH^-$ and $CO_3^{2-}$ was observed in the lower part of the film, as the mass transport rate could not keep up with the $OH^-$ evolution rate, thus the HER is suppressed and $CO_2RR$ is more favored. On Cu catalysts, a high pH value is beneficial to increase the competitiveness of the series of reaction paths of C–C bond coupling, thereby increasing the selectivity of the C2 products.[15,175,176] Interestingly, a unique pathway in $CO_2RR$ towards $C_2H_6$ were observed on many high surface area OD-Cu catalysts with highest FE of 37%, which was seldom observed for Cu foil.[113,165] This can be explained by the temporary trapping of $C_2H_4$ in the nanoporous structure, resulting in the sequential reduction of $C_2H_4$ to $C_2H_6$.
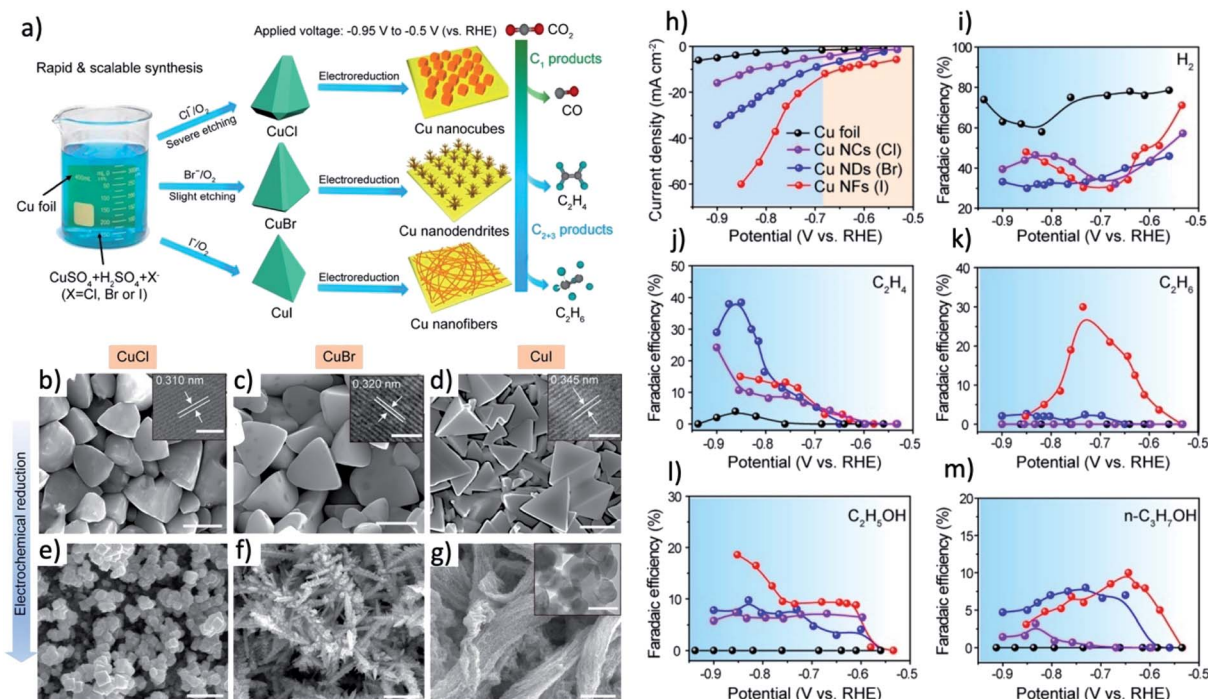
The morphology and surface area of the derived catalysts can be controlled by the reduction current, potential and choice of electrolyte. Oh and coworkers reported that pore-like Au nanostructures are produced when thin nanoporous $Au(OH)_3$ is reduced, while pillar-like Au nanostructures are formed by a faster reduction of thicker nanoporous $Au(OH)_3$.[62] The origin of these two different morphologies is associated with the electric-field-assisted transport of $Au^{3+}$ at the $Au(OH)_3$/Au interface. When the induced electric field is high on the tip of Au nanostructure, pillar-like nanostructure is formed. Instead, quasi-isotropic growth at a low electric field leads to the formation of pore-like Au nanostructures. The surface area of electrochemical synthesized OD-Ag can be tuned by changing the scanning speed of CV.[177] With higher scanning speed, the particle size of Ag samples would be smaller with high roughness factor. Lee reported that reduce the indium tin oxide nanobranches (ITO BRs) with lower current density from −1.1 mA cm$^{-2}$ to −0.48 mA cm$^{-2}$ can provide much smaller metal particles with average particle size decrease from 232 nm to 65 nm.[178] Dai and coworkers found that the particle size and roughness of halide-derived Ag can be finely tuned by changing the electrolyte and reducing the current.[70] When ethanol is used as electrolyte, the solubility of AgCl is decreased by two magnitudes compared with an aqueous solution. The mobility of $Ag^+$ is restrained, resulted in a much smaller particles size of halide-derived Ag (from 400 nm to 100 nm). Increasing the reducing current could also hinder the reorganization of Ag and further reduce the particle size to 30–50 nm.

The synthesis of pre-catalyst with high surface area can further enhance the roughness of the final derived catalysts and even control the final morphology of derived catalysts.[179] Many kinds of nanostructured $CuO_x$ and mixed metal oxides were intentionally designed to form nano/microstructured Cu catalysts with high ECSA, resulting in a $CO_2RR$ current much higher than that of the planar Cu counterparts.[16,47,180,181] Graphene-like ultrathin nanosheet morphology of Bi (Bi-ene) was successfully synthesized by Cao and coworkers from reducing of ultrathin Bi-MOLs.[37] The thickness of Bi-ene is ranging from 1.28 to 1.45 nm. The formate formation on Bi-ene starts at −0.58 V and reach near 100% selectivity between −0.83 V and −1.18 V. Similarly, special dendritic or multiple-scale-porous nanostructured Cu and Ag catalysts can be derived from MOF with hollow, nanowires and nanoboxes morphologies.[145,153,182] Most interestingly, the halide ions in electrolyte can be employed to react with Cu and tune the morphology of pre-catalyst and derived catalysts.[72–74,106] Li and coworkers found that by immersing Cu foil in the aqueous solution of corresponding halide salts (NaCl, KBr, or KI) for 5 min, cuprous halides with well-controlled tetrahedral shapes can be formed, as shown in Fig. 8a–g.[106] Specifically, the degree of truncation at both edges and vertices become lower and sharper from $Cl^-$ to $I^-$ electrolyte, and uniform cubes with a size of around 800 nm, dendrite-like nanostructures and bundles of nanofibers are formed after electroreduction, respectively. These special morphologies may contribute to the high $C_2H_4$ selectivity on Cu–Br and Cu–Cl and the unique selectivity toward $C_2H_6$ of 30% on Cu–I, as shown in Fig. 8j–m.

### 4.1. Grain boundaries and undercoordinated surface sites in derived catalysts

Although introducing nanostructures can increase the geometrical surface area for $CO_2RR$, the enhancement of $CO_2RR$ selectivity and ECSA normalized $CO_2RR$ partial current can not be simply explained by enhanced geometrical surface area. The determination of the real active sites is crucial to understand the underlying mechanism of the unique performance of compound-derived catalysts. In Kanan's research, based on SEM and TEM characterizations, it is clear that the OD-Cu is composed of the stacking of nanoparticles, with interconnecting grain boundaries.[16–18] A quantitative relationship between the density of grain boundaries (GBs) and $CO_2RR$ activity of OD-Cu and OD-Au were first revealed by Kanan group.[183,184] To control the density of GBs, Cu or Au nanoparticles were deposited on carbon nanotube (CNT) by e-beam evaporation and a subsequent annealing process was conducted. The annealing process at high temperatures can gradually decrease the GB density while leaving the general morphology unchanged. For instance, the total GB surface density was 49.5 μm$^{-1}$ for the as-deposited Au sample and the GB density can be tuned to 28.1, 13.3 and 4.2 μm$^{-1}$ by annealing at 200, 300, and 400 °C, respectively. It is found that the relationship between

**19520** | *J. Mater. Chem. A*, 2021, **9**, 19508–19533

This journal is © The Royal Society of Chemistry 2021

**Fig. 8** (a) Scheme of the facile synthesis of CuCl, CuBr, and CuI microcrystals and the corresponding Cu nanostructures after electrochemical reduction which lead to different selectivity of $CO_2$ electrochemical reduction. (b–d) SEM images of as-synthesized CuCl, CuBr, and CuI microcrystals (e–g) SEM images of Cu nanocubes, nanodendrites and nanofibers electrochemically reduced from (a)–(c), respectively. Scale bars: 2 μm. (h) $CO_2$RR current densities of Cu foil, Cu nanocubes (Cl), Cu nanodendrites (Br), and Cu nanofibers (I). (i). Faradaic efficiencies of by-product $H_2$. (j–m) Faradaic efficiencies of valuable product of $C_2H_4$, $C_2H_6$, $C_2H_5OH$, and $n$-$C_3H_7OH$. Adapted with permission from ref. 106 Copyright © 2019, American Chemical Society.

the specific $j_{CO}$ and GB surface density was linear across all Cu samples or Au samples. Moreover, at a low overpotential of 200–400 mV, all the normalized $j_{CORR}$ *vs.* density of GBs curves showed intercepts very close to 0, suggesting that the density of GBs was the only factor in this research to influence the CORR activity.

Temperature-programmed desorption (TPD) of CO on OD-Cu indicated the presence of surface sites with strong CO binding strength is correlated to the high CO reduction activity, which can be ascribed to the disordered surfaces at GB.[183] It is showed that a high-temperature feature centered at 275 K is observed for OD-Cu, which is distinct from the profile found on polycrystalline Cu.[183] Annealing the OD-Cu to 350 °C reduced the area of the high-temperature feature. When plotted the high-temperature feature against electrochemical activity, a linear correlation is obtained between surface area-corrected $j$ and the percentage of strong CO binding sites.

Kanan group performed spatially resolved measurements to elucidate the active regions at GB surface terminations of Au.[19,185] The density and profile of GBs are resolved by electron backscatter diffraction (EBSD) in a SEM and a lower potential is chosen to ensure that the $CO_2$-to-CO reduction reaction occurs solely on the GBs. Scanning electrochemical cell microscopy (SECCM) was used to probe the local electrocatalytic activity across GBs, which provide a hopping-mode current profiles with a resolution of 500 nm step size. After that, Kanan group further developed high-resolution SECCM (diameter of droplet

≈ 200 nm) and high-resolution EBSD to probe the physical origin of this enhancement on grain boundaries, as shown in Fig. 9a–c.[185] Under Ar saturated electrolyte, a step of current can be observed when scanning from one grain to the neighbouring grain, indicating a difference in HER activity between two grain surfaces. In contrast, under $CO_2$ saturated electrolyte, the currents on two grains are similar, but a much higher current peak is shown for the GB region, as shown in Fig. 9d–g. The results indicated that the GB surface terminations in Au electrodes are more active than the grain surface for $CO_2$RR. They also found that regions of enhanced $CO_2$ electroreduction activity are not correlated with lattice strain but coincident with the geometrical dislocation content. The dislocations can increase the density of undercoordinated sites which can enhance $CO_2$ electroreduction but have little impact on the hydrogen evolution activity. The accumulation of dislocations in the region of grain boundary is the likely origin of grain-boundary-enhanced $CO_2$RR activity observed previously. Another research on electrodeposited copper with *in situ* XAFS and *in situ* ECSEM revealed that the formation of reduced copper on copper surface could trigger a surface reconstruction for a rougher surface that contains abundant uncoordinated sites,[186] indicating that the effect of uncoordinated sites may actually impact the performance of all metals that vulnerable to oxidation in air or during the open circuit.

Goddard and coworkers calculated the effects of GB on OD-Cu for CORR activity through DFT calculations.[187] The results
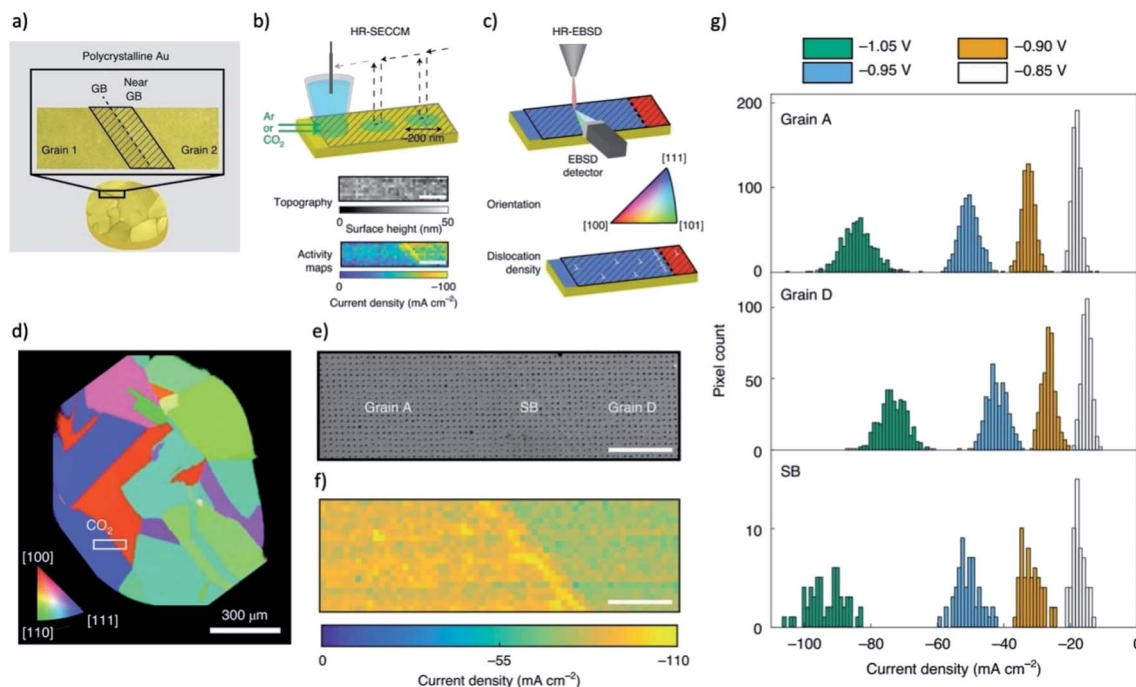
Fig. 9 (a) A typical structure of grain boundary probed by correlative SECCM and HR–EBSD measurements. (b) Illustration of voltammetric SECCM and (c) Schematic of HR–EBSD grain mapping on polycrystalline Au surface. (d) An EBSD orientation map of a typical polycrystalline Au sample viewed along the z direction. White rectangle indicates the location of the SECCM scan. (e) SEM map of the region scanned with SECCM, showing residues left from droplet contact points. (f) The current density measured from SECCM at −1.05 V *versus* Ag/AgCl. (g) Histograms of current densities from all of the pixels in grain and grain boundary regions. The scale bars in (c)–(e) are 5 μm. Adapted with permission from ref. 185 Copyright © 2021, Springer Nature.

showed that 9% of the surface sites have binding energies larger than three typical facets of (111), (100) and (211). Further calculation for the energy barrier of *OCCOH formation revealed that not all strong CO binding sites were active for C2 formation, but only the strong CO binding sites with at least one under-coordinated neighbor square site adjacent to a subsurface stacking fault could promote C–C coupling.

The GB effect was also observed on other metal oxides, such as $SnO_x$ and $BiO_x$. Lou and coworkers reported the ultrathin sub-2 nm $SnO_2$ QWs composed of separate QDs with GBs on the surface which show significantly higher current density as compared to $SnO_2$ NPs.[89] Li and coworkers found that by creating more GBs on Sn-NWs with acid etching, the current density would increase by 12 times at −1.0 V,[109] while the surface area of acid-etched Sn-NW catalyst is only 6 times higher than untreated Sn-NW. Li and coworkers synthesized a group of $Bi/Bi_2O_3$ nanosheets catalysts and found that catalysts with higher GBs actually exhibited higher partial current density and larger FE (>90%) at all applied potential range for formate production compared with samples with larger ECSA.[188]

Many specially designed pre-catalysts can also create abundant vacancies after reduction. Sargent and coworkers reported Au–S and Pb–S catalysts with obvious vacancies on the surface.[29] By decreasing the particle size from 5 nm to 3 nm, the density of vacancies increased from 5% to 20%. After 1.5 h $CO_2RR$, all pre-catalysts were converted into metallic state with much lower metal coordination numbers and enlarged bonding distance

compared with commercial metal nanoparticles. This vacancies-induced modification of electric structure significantly increases the current densities of electrosynthesis of formate, carbon monoxide on Pb and Au at low potentials of −0.2, −0.3 V. The same group also reported pre-catalyst of asymmetric paddle-wheel Cu dimer of HKUST-1,[36] which can derive into Cu clusters during $CO_2RR$. The *in situ* EXAFS showed that the average Cu–Cu coordination number of Cu cluster was reduced to 9.5 ± 0.9. The $C_2H_4$ FE was further enhanced up to 45% with the current density of 262 mA cm$^{-2}$ at −1.07 V, which is consistent with the general opinion that undercoordinated edge and corner sites on Cu surfaces are more active for C–C coupling. Li and coworkers studied the reduction of $Bi_2O_3$ NTs by EXAFS method, and they found that the coordination number of Bi–Bi is determined to be 2.6 ± 1.8 at −0.24 V, significantly smaller than that of Bi metal foil (CN = 6).[23] The $FE_{HCOOH}$ of this low-coordinated Bi catalyst can reach >93% in H-cell and 98% in a flow cell. It is reported that the $O_2 + H_2$ plasma-treated Ag showed the highest density of defects and the highest CO evolution activity, while the Ar and $H_2$ plasma-treated samples exhibited much inferior CO evolution activity although they have similar roughness.[108]

### 4.2. Surface orientation reconstruction during $CO_2RR$

The surface orientation of metal catalysts is crucial for the tuning of activity and selectivity during $CO_2RR$, particularly on copper catalyst which can drive the further reduction from the

19522 | J. Mater. Chem. A, 2021, 9, 19508–19533

This journal is © The Royal Society of Chemistry 2021

key intermediate product of CO to valuable C2+ products. Hori group and other researchers investigated the effect of crystal surface orientation of Cu on the $CO_2RR$ and CORR activity, whose results have been confirmed by many other research groups. The results found that the generation of $C_2H_4$ is more favored on Cu(100) facet relative to Cu(111) facet.[15,189,190] Specifically, the production of $CH_4$ and $C_2H_4$ from CO reduction share the same trend on Cu(111), and have a very negative onset potential of −0.8 V, as shown in Fig. 10a. Although these reaction pathways of CO reduction also existed on Cu(100), another low potential reaction pathway for the production of $C_2H_4$ from CO reduction on Cu(100) is observed at −0.45 V (Fig. 10b), indicating a highly active structure on the Cu(100) surface for $C_2H_4$ evolution. Moreover, the formation of $C_2H_4$ can be further enhanced and the evolution of $CH_4$ will be suppressed by introducing (111) steps to the Cu(100) basal plane.[189] Jiao and coworkers further found that the Cu(111) facet can manipulate the reaction pathway of CO reduction to acetate rather than $C_2H_4$.[191] This facet-related performance of $CO_2RR$ has also been observed for other metal catalysts. For instance, Luo and coworkers reported that triangular Ag nanoplates with the dominated facet of Ag(100) exhibited enhanced current density and significantly improved faradaic efficiency (96.8%) compared with normal Ag nanoparticles.[192] Woo and coworkers selectively synthesized hierarchical hexagonal Zn catalyst and found that Zn (101) facet was favorable to CO formation whereas Zn (002) facet favored the $H_2$ evolution.[193] During CO reduction reaction, many experiments also observed that the surface orientation of metal catalysts was evolving during the reduction and greatly influenced the selectivity.[194–198] A stepwise surface reconstruction of copper under certain applied potential in the electrolyte is observed by the *operando* EC-STM of Soriaga group.[194] This experimental phenomena trigger the motivation to generate a stepped Cu(S)-[3(100) × (111)], or the Cu (511) surface on Cu electrode through oxidation–reduction cycling, resulting in a FE for ethanol up to 100%.[195,196] For the surface facet regulation in $CO_2RR$, Nilsson and coworkers reported that Cu nanocube sample could be synthesized by CV scanning in $KHCO_3$ and KCl mixed electrolyte, and the sample was expected to expose dominated (100) facet and was confirmed to nearly complete suppress methane formation at potentials more negative than −0.6 V.[197] Yang and coworkers reported that the ensemble of Cu nanoparticles might go through a structural transformation process during initial electrolysis to form cube-like particles.[199] Sargent and coworkers proposed a strategy to preferentially expose and maintain Cu(100) facets by *in situ* depositing copper under $CO_2$ reduction conditions.[198] The resulted copper sample exhibited a high $FE_{C2+}$ of 90% at 520 mA cm$^{-2}$.

The evolution of pre-catalysts during $CO_2RR$ is always accompanied by dramatic structure change, thus it is natural to consider it as a potential method to control the exposed facet of
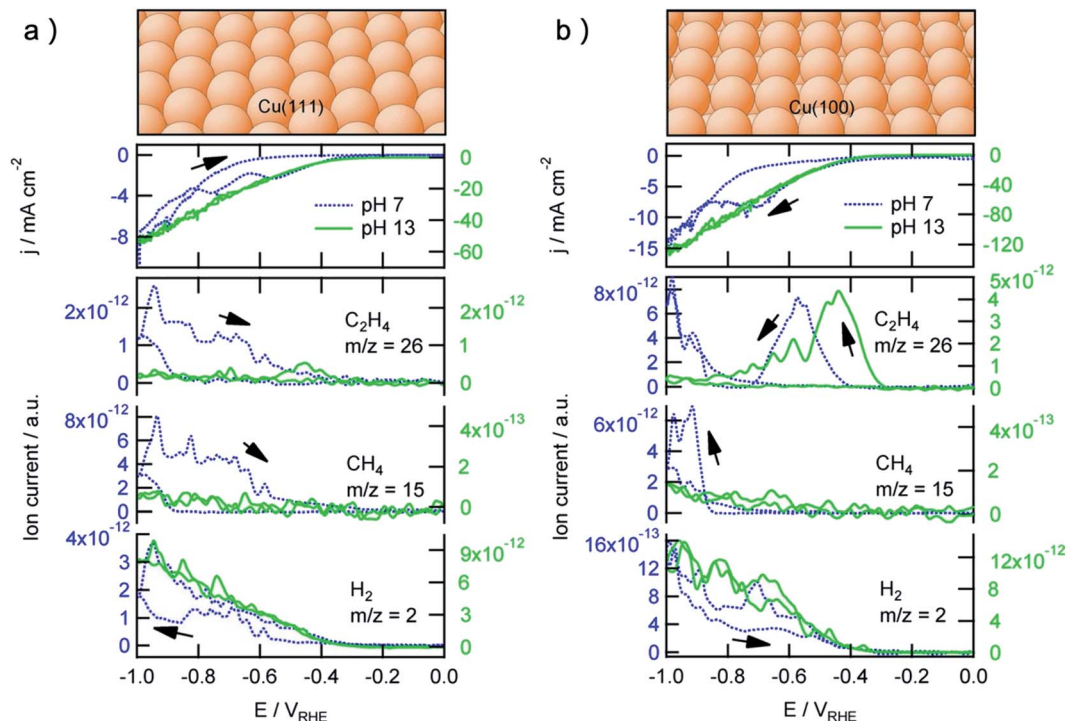


**Fig. 10** (a) Top: (111) facet of the copper fcc crystal. Middle: The catalytic current measured by cyclic voltammograms for the reduction of a saturated solution of CO (~1 mM) on Cu(111) in phosphate buffer (pH 7) and NaOH solution (pH 13). Bottom: Products of CO reduction at different potential measured by online electrochemical mass spectrometry. (b) Top: (100) facet of the copper fcc crystal. Middle: The catalytic current measured by cyclic voltammograms for the reduction of a saturated solution of CO (~1 mM) on Cu(100) in phosphate buffer (pH 7) and NaOH solution (pH 13). Bottom: Products of CO reduction at different potential measured by online electrochemical mass spectrometry. Adapted with permission from ref. 15 Copyright © 2012, American Chemical Society.

This journal is © The Royal Society of Chemistry 2021

*J. Mater. Chem. A*, 2021, **9**, 19508–19533 | **19523**

resulted catalysts. For the metal oxide pre-catalysts for $CO_2RR$, $Cu_2O$ films with [100], [110] and [111] orientation have been prepared to investigate the effect of crystal orientation on selectivity and the results showed that the final performance is not dependent on the initial crystal orientation of the catalysts.[113] Sartin *et al.* also revealed that less than 20% difference in the coverage of adsorbed CO on the shape-controlled $Cu_2O$ nanoparticles with different initially exposed crystal planes could be found. The similar coverage for different $Cu_2O$ nanoparticles implied that a surface reconstruction occurred during $CO_2RR$, resulting in a similar morphology for the OD-Cu catalysts.[200] Cuenya and coworkers synthesized $Cu_2O$ and monitored the whole reducing process with liquid cell TEM.[201] They found that the fast and extensive restructuring of $Cu_2O$ cube to Cu dendrites in 4 min. The experiments of Strasser group also confirmed that the initial cube shape and (100)-rich facet structure of $Cu_2O$ had been totally degraded during the initial reduction.[202]

Although the initial morphology of pre-catalysts may not be effective in regulating the final surface orientation of derived catalysts, there were still a few works reported some useful information of the preferable facet after pre-catalysts reduction. For OD-Cu that favor the production of C2 products, XRD test indicated that the activated Cu catalysts showed a greater abundance of (100) facets after the electrochemical $Cu_2O$ reduction, distinct from the (111) orientation that contributes to $CH_4$ products on Cu foil.[165] *Operando* ATR-SEIRAS investigations on OD-Cu particles also suggest that they possess distinct CO binding sites aside from those present on the p polycrystalline Cu surface.[203] In addition to bands similar to those on polycrystalline Cu (2073, 2089, and 2131 cm$^{-1}$), a prominent band at 2058 cm$^{-1}$ is observed in ATR-SEIRAS, corresponding to the CO adsorption band observed on the Cu (100) surface at a similar potential reported by Hori *et al.*[204]

For Ag foil and nanoparticle catalysts, (111) facet is the most stable surface orientation, however, Smith group discovered that the ratio (220) over (111) is higher after the oxidation–reduction process on Ag.[21] The single crystal facet of (110) has been reported to be more active than (111) facet for $CO_2RR$ and could be one of the reasons that OD-Ag has improved selectivity towards CO production.[205] Zhou *et al.* also found that after the Ag foil anodization, the (220) peak intensity became significantly stronger on OD-Ag.[64] For OD-Ag samples with different electrochemical anodization potential and total charge, the CO faradaic efficiency of resulted catalysts were substantially increased with enhancing (220)/(111) peak intensity ratio. Although the preferred (220) orientation and thin AgO$_x$ layer are strongly related to the high activity and selectivity of OD-Ag, the
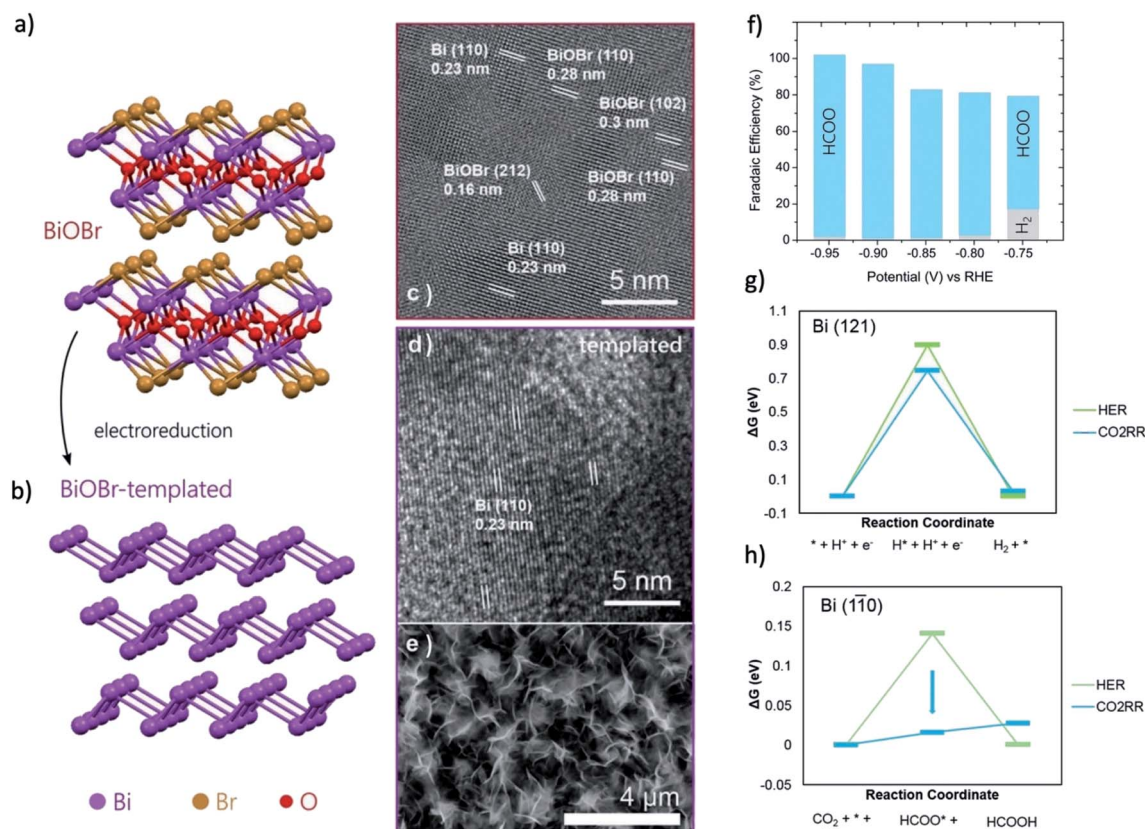


Fig. 11 Atomic structure of (a) BiOBr and (b) BiOBr-templated Bi catalyst after electroreduction. HRTEM of BiOBr (c) before and (d) after electroreduction reveal the selective reconstruction into Bi. (e) SEMs of samples after reaction reveal a 2D petal-like layered arrangement. (f) $CO_2RR$ product distribution of BiOBr-templated catalyst for different operating potentials. Formate is the only product at <−0.75 V. (g and h) The reaction energy diagram for HER and $CO_2RR$ on Bi (121) and Bi (110) facets. Adapted with permission from ref. 152 Copyright © 2018, Wiley-VCH.

19524 | *J. Mater. Chem. A*, 2021, **9**, 19508–19533

This journal is © The Royal Society of Chemistry 2021

mechanism of the forming of (220) orientation on OD-Ag sample is not clear and needs to be further investigated.

Bi-halide and Bi-salt pre-catalysts are quite unique because they can form a series of nanosheet morphology with a single exposed facet, which was observed to influence the final morphology of the derived catalysts. For instance, Luo and coworkers reported that by reducing the BiOI nanosheet precursors, Bi catalysts with nanosheet morphology can be obtained.[169] Moreover, the exposed facet of (100) or (001) on BiOI nanosheets can determine the final morphology of the Bi nanosheet to be mesoporous Bi nanosheets with inter-connected nanoparticles or Bi nanosheets with a smooth surface, respectively. Zou and coworkers reported that the $Bi_2O_2CO_3$ nanosheet mainly exposed the (001) facets would determine the orientation of the derived Bi nanosheet, resulting in the formation of Bi nanosheets that terminated with (001) facets.[105] This Bi nanosheet could exhibit a $FE_{HCOOH}$ of 90% at a low overpotential of 420 mV. Sargent and coworkers studied the BiOBr pre-catalysts by *in situ* XANES, EXAFS and GIWAXS.[152] During the $CO_2RR$, from GIWAXS experiments, the Bi (110) facet is emerged as the dominant facet during $CO_2RR$, as shown in Fig. 11a–e. The $CO_2RR$ experiment showed that the BiOBr catalyst exhibit more than two times current density compared with the Bi nanoparticle and the formate FE could reach 99% in the range of −0.8 to −1.0 V (Fig. 11f). DFT calculations in Fig. 11g and h pointed out that the Bi (110) facet can greatly lower the energy barrier of $CO_2RR$ and the stepped Bi (110) surface can offer a near-optimal Gibbs free binding energies for HCOO* (−0.01 eV). These results indicated that an atomic-level structural modification of the catalysts surface can be employed as a powerful means to regulate the product distribution for $CO_2RR$.

# 5. Stability of the $CO_2$ pre-catalysts

The stability is a universal challenge for all $CO_2RR$ catalysts, which originated from the impurities in the solution and the evolution of catalysts.[206] The former challenge can be resolved using an ultra-pure electrolyte, chelating agent, or high surface area catalysts with alkaline electrolyte,[207–210] while the under-standing of the later challenge is still preliminary and the solution is yet to develop.

One major evolution process of $CO_2RR$ catalysts is the morphology evolution, such as the stepwise surface recon-struction of copper under certain applied potential region,[194] and the forming of Cu cube under CV scans[197] mentioned above. There are also many experiments found that the high activity morphology suffered from degradation under long-term operation. Cuenya and coworkers reported that for copper cubes deposited on carbon, the Cu(100) facets became rougher



**Fig. 12** The interface energies of (a) H-covered and (b) CO-covered Cu surfaces of (111), (100) and (110). (c) The equilibrium of Wulff-shape of Cu nanoparticle based on the calculation of interface energies. (d) Schematic illustration of the degradation mechanism of Cu NCs during $CO_2RR$. The degradation mechanism that includes nanoclustering (stage I) followed by a coalescence at a later stage (stage II). Adapted with permission from ref. 212 Copyright © 2018, Springer Nature.

This journal is © The Royal Society of Chemistry 2021

*J. Mater. Chem. A*, 2021, **9**, 19508–19533 | **19525**

and losing the cubic shape, resulting in a suppression of multi-carbon products (*i.e.*, $C_2H_4$ and ethanol) *versus* $CH_4$.[211] Buonsanti and coworkers found that at a sufficiently negative potential, the nanoparticle of metal catalysts were reshaped and formed nanocluster to expose the surface facet with a lower adsorption energy of either H- or CO-species on the catalyst surface (Fig. 12a–c). This reshaping was the reason for the unavoidable degradation of the crystals, and small crystals were more vulnerable to degradation (Fig. 12d).[212] The pre-catalysts-derived catalysts benefit from a relatively high surface area and nanostructure, which are also vulnerable to the structure evolution under long-term operation. For instance, during $CO_2RR$, the OD-Au seems to be sintered over time, resulting in decreased current density and FE. Specifically, a roughness factor of 72 was reduced to 17 after 8 h operation, indicating that sintering of Au NPs occurred during $CO_2$ reduction electrolysis.[18] SEM and PXRD line-broadening analysis of these electrodes after 8 h showed an increase in particle and crystallite size over time, consistent with the observed RF decrease. In another research, ECSA measurements performed after 12 h of $CO_2$ electrolysis reaction showed that the surface areas of OD-Au decrease from 8.3 to 5 $m^2$ $g^{-1}$, respectively, in good agreement with SEM observations.[63] However, it is important to note that $FE_{CO}$ for OD-Au stays relatively constant at about 90% even after running for 12 h, thus implying that the feature size alone cannot explain the better performance of OD-Au. The $CO_2RR$ efficiency towards CO also degrades slightly after 3 h of reaction on the oxidized Ag samples because of a slight decrease in current towards CO and a growth in the HER current.[108] This time-dependent change is likely related to the change in surface structure over the course of the reaction observed by SEM images. Electrochemical surface roughness measurements also indicate that the roughness of the surface decreases by approximately half between 1–3 h of reaction.

The long-term existence of nonmetal elements in the derived catalysts during $CO_2RR$ is highly suspicious due to the relatively high standard electrode potential compared with $CO_2RR$. Obviously, the voltage of catalytic reduction has a great influence on the retention of nonmetallic components, evidenced by the clear transition from $SnO_2$ to Sn when changing the potential from 0.1 V to −0.7 V.[123] This phenomenon emphasizes the importance of studying the structure and composition change of pre-catalysts in flow cell which usually adopt much higher voltage and current compared with H-cell. On the other hand, the low conductivity metal compounds pre-catalysts may be in an electrochemically inactive state after the surrounding parts are reduced to metal.[179] This could also be part of the reason for the remnant of nonmetal elements under the surface of catalysts. However, based on currently released data, one can not confirm that the nonmetal content will remain at a relatively stable value rather than a continuous decline under the condition of long-term work with even low overpotential.

Currently, the stability of derived catalysts is not properly studied, because most studies do not have long-term test and no structural test after a long-term operation is carefully and detailly characterized. Ager and coworker reported that only a small fraction (<1%) of the original O content remains after $CO_2RR$ of 10 min, however, the FE of ethylene could be maintained at 35% for 5 h.[137] Gong and coworkers' research, on the other hand, showed that the $Cu^+$ can be stabilized in $Cu/CuSiO_3$ and the $FE_{C2H4}$ of catalyst remained 50% for 6 h.[213] These studies indicated that the derived catalysts can catalyze the $CO_2RR$ with a relative stable structure, however, slow structure evolution of derived catalysts cannot be excluded if longer testing period is applied. The prolonged $CO_2RR$ test of Han and coworkers on Au sulfide catalysts showed a relatively stable performance for the first 6 h and a clear decline of CO selectivity between 6 and 10 h.[214] An even longer test of 72 h had been applied to Ag–Cl pre-catalyst by Polyansky and coworkers.[32] They found that the morphology of catalysts was dramatically changed, resulting in 20–30% decrease of electrochemical surface area and current density. Moreover, the relationship



Fig. 13 (a) The scheme of regeneration of $Cu^+$ by pulsed electrolysis strategy. (b) Atomic force microscopy images of a Cu(100) electrode after 1 h of alternative pulsed electrolysis of $E_a$ = 0.6 V, $E_c$ = −1.0 V, $t_a$ = $t_c$ = 1 s. The Cu(100) electrode was transformed to cubic islands with (100) facets. (c) Quasi *in situ* copper LMM Auger spectra of a Cu(100) electrode after the different pulse protocols. Larger amount of $Cu_2O$ can be observed on sample with higher $E_a$. (d) The bar chart of product selectivity for different pulse protocols. Adapted with permission from ref. 24 Copyright © 2020, Springer Nature.

**19526** | *J. Mater. Chem. A*, 2021, **9**, 19508–19533

This journal is © The Royal Society of Chemistry 2021

between $CO_2RR$ selectivity and morphology changes may not be linear. One research indicated that the deactivation of OD-Cu process might affect long-chain products (C3–C4) first and the C2 selectivity could be relatively stable during first several hours.[140] It is reported that the $Cu_2OCl$ exhibited a stable productivity toward $C_2H_4$ and $C_2H_5OH$ over a period of 7 hours, while the productivity of C3–C4 products are dramatically decreased due to the decreasing relative ratio of $Cu^+$ to $Cu^0$.

The dilemma between short lifetime and high activity of $Cu^+$ ions in $CO_2$ reduction catalyst triggers the efforts to regenerate copper oxide during catalysis. Cuenya and coworkers proposed an alternative pulsed electrolysis strategy to regenerate the Cu(I) ions at a positive potential,[24] as shown in Fig. 13a. This regeneration strategy can help to reshape the surface morphology of Cu to nanocube and maintain a high concentration of $Cu_2O$ (Fig. 13b and c). Specifically, significantly enhanced selectivity for ethanol (32%) has been found under alternative pulsed electrolysis conditions of 0.6 V and −1.0 V due to the co-existence of Cu(I) and Cu(0) species created by an anodic pulse (Fig. 13d).[24] Another research showed that the alternating voltage method is better at providing a large selection of oxygenated hydrocarbons products compared with cyclic voltammetry and chronoamperometric methods.[215] Besides anodic pulse, keeping catalyst at open circuit potential can also help the regeneration of copper oxides and prolong the product selectivity towards $C_2H_4$.[216]

# 6. Summary and perspective

The pre-catalyst system showed impressive performance in $CO_2$ reduction. Elements such as O, N, S, and Cl are believed to significantly increase the valence of metals, and the loss of them in the *in situ* environment will introduce specific structural defects to the catalyst system. Generally, the pre-catalyst strategy does not change the species of products on certain metal catalysts but greatly improve the reaction rate and distribution of products. One universal benefit for all pre-catalysts is the suppression of hydrogen evolution because the rough surface of derived catalysts can maintain a high pH environment during $CO_2RR$ to hinder the supply of proton for HER.[171–173] The reduction of pre-catalyst can also create under-coordinated reaction sites on the catalysts surface. For instance, the Au–O pre-catalysts can greatly improve the $FE_{CO}$ to 99%, which attribute to the enhanced surface area and abundant surface under-coordinated reaction sites.[18,19,185] However, the facile control of morphology and the density of grain boundaries for improved $CO_2RR$ activity is not yet realized. The concentration of nonmetal element remained in derived catalysts was more systematically studied and was found to be strongly related with the $CO_2RR$ activity. For Cu–O and Ag–O pre-catalysts, the sample with higher O content were found to be more efficient for C2+ and CO production, respectively.[21,157] For HCOOH producing catalysts, such as Sn, it was found that the partially oxidized metal ions on catalyst surface have much higher activity than pure metal or metal oxides.[22,123] S-contained pre-catalyst is the most special one among all other pre-catalysts because it can tune the selectivity of copper to pure HCOOH,

and the sulfiding of many non-active metals can result in active CO or HCOOH producing catalysts such as $WSe_2$, $TiS_2$, In–S.[78,80,104,147,148] The copper-nonmetal compound, such as Cu–B, Cu–N, Cu-halide,[30,31] attracted intense attention recently due to its ability to significantly enhance the FE of C2+ products. Notably, the average oxidation states of copper in the X–Cu catalysts is proportional with the electronegativity of the halogen, and F–Cu catalyst showed the best C2+ FEs and highest surface area normalized C2+ formation rates among all Cu-halide samples. Comparing the $CO_2RR$ selectivity of Cu-based pre-catalysts with different nonmetal elements is very important and yet to realize. Generally, the current overall research is still in a very rough stage, lacking guiding theories and systematic rules. Thus, the following challenges should be considered and addressed to push the $CO_2RR$ pre-catalysts strategy technique forward.

(1) The *in situ* activation process of the pre-catalyst is very complicated, accompanied by the change of the metal valence and the change of the overall morphology of the catalyst. Therefore, it is just an assumption to attribute the origin of catalyst performance to one of the structure or composition factors. Some studies simply studied a specific element ratio or specific morphology of the pre-catalyst, which is very difficult to obtain an in-depth understanding of the catalytic activity. Other research works were conducted by controlling the ratio of elements, or controlling the changes of certain structural parameters, thus, they can provide more valuable conclusions on the influence of certain parameter. In future research, we should consider separating these structural parameters more clearly. For example, one could control the size and distribution of the pre-catalyst particles on an inert substrate so that it will not form a special macroscopic morphology. With this platform one can focus on the effect of nonmetals on the performance of metal catalysts.

(2) An efficient $CO_2RR$ catalyst for large scale application should possess a long lifetime of >1 year even under high reaction rate. However, the composition and morphology of catalysts evolved from the pre-catalysts is more likely to be a metastable state and may keep evolving during electrolysis. Therefore, it is particularly important in the future research to conduct *in situ* or quasi-*in situ* tests of long-term $CO_2RR$ operation to probe the mechanism of structural evolution. The current research usually focused on the operation period of <5 hours which may not show the effect of structure changes on the performance. Several studies that performed long term stability test such as 10 h or 72 h clearly revealed a structure evolving and the dropping of $CO_2$ reduction efficiency.[32,214] Operation-regeneration cycle is confirmed to be a promising approach to prolong the unique $CO_2$ reduction activity on $CuO_x$, however, the regeneration strategy for other pre-catalysts is still lacking. To realize a strategy that can regenerate metal–nonmetal compound pre-catalysts *in situ* under working conditions would be a game changer in this area.

(3) Considering the pre-catalysts have a high possibility of being transformed to metal phase through an *in situ* dynamic evolution process, it is obvious that the impurities existed in the electrolyte should also matters and can change the final

This journal is © The Royal Society of Chemistry 2021

*J. Mater. Chem. A*, 2021, **9**, 19508–19533 | **19527**

composition and activity of the catalysts. Indeed, the alkaline electrolyte may etch the stainless flow cell and release various elements to interference the ultimate activity results. On the other hand, the un-purified electrolyte also contains a lot of unexpected impurities, leading to the composition change and deactivation of catalysts. Protecting the catalyst with stable materials[217–221] or developing robust catalysts that intrinsically resistant to impurities should be designed to enhance the lifetime and maintain the activity for specific products. Alternatively, introducing chelating agent in electrolyte is another powerful way to minimize the effect of impurities during operation.[209] What's more, the optimization of configuration of flow cell to improve operation environment should be contribute to alleviate the pollution, which may can be boosted by modelling and simulation works.

(4) The researches mentioned above were basically focused on the influence of a single nonmetallic element on the final performance of the metal catalyst. Considering the unique effects of different nonmetals on the final properties of metal catalysts, the use of multiple nonmetals to jointly adjust the metal properties or the activation process will enable us to have more refined tools for adjusting the catalyst performance. Furthermore, incorporating the alloy-related research experience and introducing complicated design of the tandem structure will bring about a series of brand-new $CO_2$ reduction catalysts.

## Conflicts of interest

There are no conflicts to declare.

## Acknowledgements

## References

1 N. S. Lewis and D. G. Nocera, *Proc. Natl. Acad. Sci. U. S. A.*, 2006, **103**, 15729–15735.
2 C. Li, Q. Cao, F. Wang, Y. Xiao, Y. Li, J. J. Delaunay and H. Zhu, *Chem. Soc. Rev.*, 2018, **47**, 4981–5037.
3 C. Li, J. He, Y. Xiao, Y. Li and J.-J. Delaunay, *Energy Environ. Sci.*, 2020, **13**, 3269–3306.
4 C. Feng, M. B. Faheem, J. Fu, Y. Xiao, C. Li and Y. Li, *ACS Catal.*, 2020, **10**, 4019–4047.
5 Y. Li, W. Cheng, H. Su, X. Zhao, J. He and Q. Liu, *Nano Energy*, 2020, **77**, 105121.
6 S. Xu and E. A. Carter, *Chem. Rev.*, 2019, **119**, 6631–6669.
7 D. M. Weekes, D. A. Salvatore, A. Reyes, A. Huang and C. P. Berlinguette, *Acc. Chem. Res.*, 2018, **51**, 910–918.
8 S. Zhang, Q. Fan, R. Xia and T. J. Meyer, *Acc. Chem. Res.*, 2020, **53**, 255–264.
9 J. He, Y. Li, A. Huang, Q. Liu and C. Li, *Electrochem. Energy Rev.*, 2021, DOI: 10.1007/s41918-021-00100-y.
10 Y. Hori, in *Modern Aspects of Electrochemistry*, ed. C. G. Vayenas, R. E. White and M. E. Gamboa-Aldeco, Springer

11 J. Qiao, Y. Liu, F. Hong and J. Zhang, *Chem. Soc. Rev.*, 2014, **43**, 631–675.
12 Y. Y. Birdja, E. Pérez-Gallent, M. C. Figueiredo, A. J. Göttle, F. Calle-Vallejo and M. T. M. Koper, *Nat. Energy*, 2019, **4**, 732–745.
13 J. He, N. J. J. Johnson, A. Huang and C. P. Berlinguette, *ChemSusChem*, 2018, **11**, 48–57.
14 Y. Hori, I. Takahashi, O. Koga and N. Hoshi, *J. Mol. Catal. A: Chem.*, 2003, **199**, 39–47.
15 K. J. Schouten, Z. Qin, E. Perez Gallent and M. T. Koper, *J. Am. Chem. Soc.*, 2012, **134**, 9864–9867.
16 C. W. Li and M. W. Kanan, *J. Am. Chem. Soc.*, 2012, **134**, 7231–7234.
17 C. W. Li, J. Ciston and M. W. Kanan, *Nature*, 2014, **508**, 504–507.
18 Y. Chen, C. W. Li and M. W. Kanan, *J. Am. Chem. Soc.*, 2012, **134**, 19969–19972.
19 R. G. Mariano, K. McKelvey, H. S. White and M. W. Kanan, *Science*, 2017, **358**, 1187–1192.
20 M. Ma, B. J. Trześniewski, J. Xie and W. A. Smith, *Angew. Chem., Int. Ed.*, 2016, **55**, 9748–9752.
21 N. J. Firet, M. A. Blommaert, T. Burdyny, A. Venugopal, D. Bohra, A. Longo and W. A. Smith, *J. Mater. Chem. A*, 2019, **7**, 2597–2607.
22 Y. Chen and M. W. Kanan, *J. Am. Chem. Soc.*, 2012, **134**, 1986–1989.
23 Q. Gong, P. Ding, M. Xu, X. Zhu, M. Wang, J. Deng, Q. Ma, N. Han, Y. Zhu, J. Lu, Z. Feng, Y. Li, W. Zhou and Y. Li, *Nat. Commun.*, 2019, **10**, 2807.
24 R. M. Arán-Ais, F. Scholten, S. Kunze, R. Rizo and B. Roldan Cuenya, *Nat. Energy*, 2020, **5**, 317–325.
25 P. Deng, H. Wang, R. Qi, J. Zhu, S. Chen, F. Yang, L. Zhou, K. Qi, H. Liu and B. Y. Xia, *ACS Catal.*, 2019, **10**, 743–750.
26 T.-T. Zhuang, Z.-Q. Liang, A. Seifitokaldani, Y. Li, P. De Luna, T. Burdyny, F. Che, F. Meng, Y. Min, R. Quintero-Bermudez, C. T. Dinh, Y. Pang, M. Zhong, B. Zhang, J. Li, P.-N. Chen, X.-L. Zheng, H. Liang, W.-N. Ge, B.-J. Ye, D. Sinton, S.-H. Yu and E. H. Sargent, *Nat. Catal.*, 2018, **1**, 421–428.
27 Z. Chen, X. Zhang, M. Jiao, K. Mou, X. Zhang and L. Liu, *Adv. Energy Mater.*, 2020, **10**, 1903664.
28 Y. Zhang, F. Li, X. Zhang, T. Williams, C. D. Easton, A. M. Bond and J. Zhang, *J. Mater. Chem. A*, 2018, **6**, 4714–4720.
29 M. Liu, M. Liu, X. Wang, S. M. Kozlov, Z. Cao, P. De Luna, H. Li, X. Qiu, K. Liu, J. Hu, C. Jia, P. Wang, H. Zhou, J. He, M. Zhong, X. Lan, Y. Zhou, Z. Wang, J. Li, A. Seifitokaldani, C. T. Dinh, H. Liang, C. Zou, D. Zhang, Y. Yang, T.-S. Chan, Y. Han, L. Cavallo, T.-K. Sham, B.-J. Hwang and E. H. Sargent, *Joule*, 2019, **3**, 1703–1718.
30 P. De Luna, R. Quintero-Bermudez, C.-T. Dinh, M. B. Ross, O. S. Bushuyev, P. Todorović, T. Regier, S. O. Kelley, P. Yang and E. H. Sargent, *Nat. Catal.*, 2018, **1**, 103–110.

New York, New York, 2008, pp. 89–189, DOI: 10.1007/978-0-387-49489-0_3.

**19528** | *J. Mater. Chem. A*, 2021, **9**, 19508–19533

This journal is © The Royal Society of Chemistry 2021

31 W. Ma, S. Xie, T. Liu, Q. Fan, J. Ye, F. Sun, Z. Jiang, Q. Zhang, J. Cheng and Y. Wang, *Nat. Catal.*, 2020, **3**, 478–487.

32 Y.-C. Hsieh, S. D. Senanayake, Y. Zhang, W. Xu and D. E. Polyansky, *ACS Catal.*, 2015, **5**, 5349–5356.

33 S. He, F. Ni, Y. Ji, L. Wang, Y. Wen, H. Bai, G. Liu, Y. Zhang, Y. Li, B. Zhang and H. Peng, *Angew. Chem., Int. Ed.*, 2018, **57**, 16114–16119.

34 Z.-Q. Liang, T.-T. Zhuang, A. Seifitokaldani, J. Li, C.-W. Huang, C.-S. Tan, Y. Li, P. De Luna, C. T. Dinh, Y. Hu, Q. Xiao, P.-L. Hsieh, Y. Wang, F. Li, R. Quintero-Bermudez, Y. Zhou, P. Chen, Y. Pang, S.-C. Lo, L.-J. Chen, H. Tan, Z. Xu, S. Zhao, D. Sinton and E. H. Sargent, *Nat. Commun.*, 2018, **9**, 3828.

35 H. Li, P. Wen, D. S. Itanze, Z. D. Hood, X. Ma, M. Kim, S. Adhikari, C. Lu, C. Dun, M. Chi, Y. Qiu and S. M. Geyer, *Nat. Commun.*, 2019, **10**, 5724.

36 D. H. Nam, O. S. Bushuyev, J. Li, P. De Luna, A. Seifitokaldani, C. T. Dinh, F. P. Garcia de Arquer, Y. Wang, Z. Liang, A. H. Proppe, C. S. Tan, P. Todorovic, O. Shekhah, C. M. Gabardo, J. W. Jo, J. Choi, M. J. Choi, S. W. Baek, J. Kim, D. Sinton, S. O. Kelley, M. Eddaoudi and E. H. Sargent, *J. Am. Chem. Soc.*, 2018, **140**, 11378–11386.

37 C. Cao, D. D. Ma, J. F. Gu, X. Xie, G. Zeng, X. Li, S. G. Han, Q. L. Zhu, X. T. Wu and Q. Xu, *Angew. Chem., Int. Ed.*, 2020, **59**, 15014–15020.

38 Y. Zhou, F. Che, M. Liu, C. Zou, Z. Liang, P. De Luna, H. Yuan, J. Li, Z. Wang, H. Xie, H. Li, P. Chen, E. Bladt, R. Quintero-Bermudez, T. K. Sham, S. Bals, J. Hofkens, D. Sinton, G. Chen and E. H. Sargent, *Nat. Chem.*, 2018, **10**, 974–980.

39 B. R. Wygant, K. Kawashima and C. B. Mullins, *ACS Energy Lett.*, 2018, **3**, 2956–2966.

40 A. Bergmann and B. Roldan Cuenya, *ACS Catal.*, 2019, **9**, 10020–10043.

41 S. W. Chee, T. Lunkenbein, R. Schlögl and B. R. Cuenya, *J. Phys.: Condens. Matter*, 2021, **33**, 153001.

42 J. Timoshenko and B. Roldan Cuenya, *Chem. Rev.*, 2021, **121**, 882–961.

43 L. Trotochaud, S. L. Young, J. K. Ranney and S. W. Boettcher, *J. Am. Chem. Soc.*, 2014, **136**, 6744–6753.

44 M. S. Burke, S. Zou, L. J. Enman, J. E. Kellon, C. A. Gabor, E. Pledger and S. W. Boettcher, *J. Phys. Chem. Lett.*, 2015, **6**, 3737–3742.

45 M. S. Burke, L. J. Enman, A. S. Batchellor, S. Zou and S. W. Boettcher, *Chem. Mater.*, 2015, **27**, 7549–7558.

46 P. Chen, Y. Jiao, Y.-H. Zhu, S.-M. Chen, L. Song, M. Jaroniec, Y. Zheng and S.-Z. Qiao, *J. Mater. Chem. A*, 2019, **7**, 7675–7682.

47 M. Nur Hossain, S. Chen and A. Chen, *Appl. Catal., B*, 2019, **259**, 118096.

48 Y. Lum, B. Yue, P. Lobaccaro, A. T. Bell and J. W. Ager, *J. Phys. Chem. C*, 2017, **121**, 14191–14203.

49 L. Chen, F. Li, C. L. Bentley, M. Horne, A. M. Bond and J. Zhang, *ChemElectroChem*, 2017, **4**, 1402–1410.

50 C. I. Shaughnessy, D. T. Jantz and K. C. Leonard, *J. Mater. Chem. A*, 2017, **5**, 22743–22749.

51 C. Yan, L. Lin, D. Gao, G. Wang and X. Bao, *J. Mater. Chem. A*, 2018, **6**, 19743–19749.

52 J. Wu, F. G. Risalvato, S. Ma and X.-D. Zhou, *J. Mater. Chem. A*, 2014, **2**, 1647–1651.

53 C. Chen, X. Sun, L. Lu, D. Yang, J. Ma, Q. Zhu, Q. Qian and B. Han, *Green Chem.*, 2018, **20**, 4579–4583.

54 Y. Mi, S. Shen, X. Peng, H. Bao, X. Liu and J. Luo, *ChemElectroChem*, 2019, **6**, 2393–2397.

55 M. Ebaid, K. Jiang, Z. Zhang, W. S. Drisdell, A. T. Bell and J. K. Cooper, *Chem. Mater.*, 2020, **32**, 3304–3311.

56 J. Szlachetko, J. Sa, M. Nachtegaal, U. Hartfelder, J. C. Dousse, J. Hoszowska, D. L. Abreu Fernandes, H. Shi and C. Stampfl, *J. Phys. Chem. Lett.*, 2014, **5**, 80–84.

57 L. K. Ono and B. Roldan Cuenya, *J. Phys. Chem. C*, 2008, **112**, 4676–4686.

58 G. B. Hoflund, Z. F. Hazos and G. N. Salaita, *Phys. Rev. B*, 2000, **62**, 11126–11133.

59 K. Jiang, P. Kharel, Y. Peng, M. K. Gangishetty, H.-Y. G. Lin, E. Stavitski, K. Attenkofer and H. Wang, *ACS Sustainable Chem. Eng.*, 2017, **5**, 8529–8534.

60 B. Tang and C. Wang, *Sci. China: Technol. Sci.*, 2018, **61**, 389–396.

61 H. Kim, H. S. Jeon, M. S. Jee, E. B. Nursanto, J. P. Singh, K. Chae, Y. J. Hwang and B. K. Min, *ChemSusChem*, 2016, **9**, 2097–2102.

62 J. Kim, J. T. Song, H. Ryoo, J.-G. Kim, S.-Y. Chung and J. Oh, *J. Mater. Chem. A*, 2018, **6**, 5119–5128.

63 Z. Qi, J. Biener and M. Biener, *ACS Appl. Energy Mater.*, 2019, **2**, 7717–7721.

64 L. Q. Zhou, C. Ling, M. Jones and H. Jia, *Chem. Commun.*, 2015, **51**, 17704–17707.

65 A. H. Shah, Y. Wang, S. Hussain, M. B. Akbar, A. R. Woldu, X. Zhang and T. He, *Phys. Chem. Chem. Phys.*, 2020, **22**, 2046–2053.

66 A. Raiyan, S. Das and M. R. Islam, *Procedia Eng.*, 2017, **194**, 276–283.

67 M. Ma, K. Liu, J. Shen, R. Kas and W. A. Smith, *ACS Energy Lett.*, 2018, **3**, 1301–1306.

68 Y. Zhang, X. Zhang, Y. Ling, F. Li, A. M. Bond and J. Zhang, *Angew. Chem., Int. Ed.*, 2018, **57**, 13283–13287.

69 W. Qiu, R. Liang, Y. Luo, G. Cui, J. Qiu and X. Sun, *Inorg. Chem. Front.*, 2018, **5**, 2238–2241.

70 L. Zhang, Z. Wang, N. Mehio, X. Jin and S. Dai, *ChemSusChem*, 2016, **9**, 428–432.

71 K. R. Phillips, Y. Katayama, J. Hwang and Y. Shao-Horn, *J. Phys. Chem. Lett.*, 2018, **9**, 4407–4412.

72 D. Gao, I. T. McCrum, S. Deo, Y.-W. Choi, F. Scholten, W. Wan, J. G. Chen, M. J. Janik and B. Roldan Cuenya, *ACS Catal.*, 2018, **8**, 10012–10020.

73 D. Gao, F. Scholten and B. Roldan Cuenya, *ACS Catal.*, 2017, **7**, 5112–5120.

74 A. S. Varela, W. Ju, T. Reier and P. Strasser, *ACS Catal.*, 2016, **6**, 2136–2144.

This journal is © The Royal Society of Chemistry 2021

*J. Mater. Chem. A*, 2021, **9**, 19508–19533 | **19529**

75 A. Basiratnia, J. Rempel, F. Li, A. Pogodaev, T. A. Zienchuk and A. Klinkova, *Phys. Chem. Chem. Phys.*, 2019, **21**, 5894–5897.

76 Y. Gao, Q. Wu, X. Liang, Z. Wang, Z. Zheng, P. Wang, Y. Liu, Y. Dai, M. H. Whangbo and B. Huang, *Adv. Sci.*, 2020, **7**, 1902820.

77 D. Yang, Q. Zhu, C. Chen, H. Liu, Z. Liu, Z. Zhao, X. Zhang, S. Liu and B. Han, *Nat. Commun.*, 2019, **10**, 677.

78 T. Shinagawa, G. O. Larrazábal, A. J. Martín, F. Krumeich and J. Pérez-Ramírez, *ACS Catal.*, 2018, **8**, 837–844.

79 Z. Yin, C. Yu, Z. Zhao, X. Guo, M. Shen, N. Li, M. Muzzio, J. Li, H. Liu, H. Lin, J. Yin, G. Lu, D. Su and S. Sun, *Nano Lett.*, 2019, **19**, 8658–8663.

80 W. Ma, S. Xie, X. G. Zhang, F. Sun, J. Kang, Z. Jiang, Q. Zhang, D. Y. Wu and Y. Wang, *Nat. Commun.*, 2019, **10**, 892.

81 B. Qin, Y. Li, H. Wang, G. Yang, Y. Cao, H. Yu, Q. Zhang, H. Liang and F. Peng, *Nano Energy*, 2019, **60**, 43–51.

82 H. Yang, N. Han, J. Deng, J. Wu, Y. Wang, Y. Hu, P. Ding, Y. Li, Y. Li and J. Lu, *Adv. Energy Mater.*, 2018, **8**, 1801536.

83 Y. Qiu, J. Du, C. Dai, W. Dong and C. Tao, *J. Electrochem. Soc.*, 2018, **165**, H594–H600.

84 F. Li, L. Chen, M. Xue, T. Williams, Y. Zhang, D. R. MacFarlane and J. Zhang, *Nano Energy*, 2017, **31**, 270–277.

85 A. Zhang, R. He, H. Li, Y. Chen, T. Kong, K. Li, H. Ju, J. Zhu, W. Zhu and J. Zeng, *Angew. Chem., Int. Ed.*, 2018, **57**, 10954–10958.

86 R. He, X. Yuan, P. Shao, T. Duan and W. Zhu, *Small*, 2019, **15**, e1904882.

87 H. Zhang, Y. Ma, F. Quan, J. Huang, F. Jia and L. Zhang, *Electrochem. Commun.*, 2014, **46**, 63–66.

88 Q. Wang, M. Ma, S. Zhang, K. Lu, L. Fu, X. Liu and Y. Chen, *ChemPlusChem*, 2020, **85**, 672–678.

89 S. Liu, J. Xiao, X. F. Lu, J. Wang, X. Wang and X. W. D. Lou, *Angew. Chem., Int. Ed.*, 2019, **58**, 8499–8503.

90 X. Li, S. Dou, J. Wang and X. Wang, *Chem.–Asian J.*, 2020, **15**, 1558–1561.

91 F. Li, L. Chen, G. P. Knowles, D. R. MacFarlane and J. Zhang, *Angew. Chem., Int. Ed.*, 2017, **56**, 505–509.

92 J. H. Zhou, K. Yuan, L. Zhou, Y. Guo, M. Y. Luo, X. Y. Guo, Q. Y. Meng and Y. W. Zhang, *Angew. Chem., Int. Ed.*, 2019, **58**, 14197–14201.

93 S. Liu, H. Tao, Q. Liu, Z. Xu, Q. Liu and J.-L. Luo, *ACS Catal.*, 2018, **8**, 1469–1475.

94 F. Y. Gao, S. J. Hu, X. L. Zhang, Y. R. Zheng, H. J. Wang, Z. Z. Niu, P. P. Yang, R. C. Bao, T. Ma, Z. Dang, Y. Guan, X. S. Zheng, X. Zheng, J. F. Zhu, M. R. Gao and S. H. Yu, *Angew. Chem., Int. Ed.*, 2020, **59**, 8706–8712.

95 Q. Wan, J. Zhang, B. Zhang, D. Tan, L. Yao, L. Zheng, F. Zhang, L. Liu, X. Cheng and B. Han, *Green Chem.*, 2020, **22**, 2750–2754.

96 Z. Geng, X. Kong, W. Chen, H. Su, Y. Liu, F. Cai, G. Wang and J. Zeng, *Angew. Chem., Int. Ed.*, 2018, **57**, 6054–6059.

97 X. Jiang, F. Cai, D. Gao, J. Dong, S. Miao, G. Wang and X. Bao, *Electrochem. Commun.*, 2016, **68**, 67–70.

98 W. Luo, Q. Zhang, J. Zhang, E. Moioli, K. Zhao and A. Züttel, *Appl. Catal., B*, 2020, **273**, 119060.

99 Y. Wang, H. Liu, J. Yu, B. Hu, H. Zhao, P. Tsiakaras and S. Song, *Electrochim. Acta*, 2019, **328**, 135083.

100 C. Li, T. Hisatomi, O. Watanabe, M. Nakabayashi, N. Shibata, K. Domen and J.-J. Delaunay, *Energy Environ. Sci.*, 2015, **8**, 1493–1500.

101 C. Li, Y. Li and J. J. Delaunay, *ACS Appl. Mater. Interfaces*, 2014, **6**, 480–486.

102 H. Ramezani, D. N. Christodoulides, V. Kovanis, I. Vitebskiy and T. Kottos, *Phys. Rev. Lett.*, 2012, **109**, 033902.

103 C. Li, H. Yamahara, Y. Lee, H. Tabata and J. J. Delaunay, *Nanotechnology*, 2015, **26**, 305503.

104 Y. Huang, Y. Deng, A. D. Handoko, G. K. L. Goh and B. S. Yeo, *ChemSusChem*, 2018, **11**, 320–326.

105 M. Zhao, Y. Gu, W. Gao, P. Cui, H. Tang, X. Wei, H. Zhu, G. Li, S. Yan, X. Zhang and Z. Zou, *Appl. Catal., B*, 2020, **266**, 118625.

106 H. Wang, E. Matios, C. Wang, J. Luo, X. Lu, X. Hu and W. Li, *Nano Lett.*, 2019, **19**, 3925–3932.

107 Y. Zhang, L. Ji, W. Qiu, X. Shi, A. M. Asiri and X. Sun, *Chem. Commun.*, 2018, **54**, 2666–2669.

108 H. Mistry, Y. W. Choi, A. Bagger, F. Scholten, C. S. Bonifacio, I. Sinev, N. J. Divins, I. Zegkinoglou, H. S. Jeon, K. Kisslinger, E. A. Stach, J. C. Yang, J. Rossmeisl and B. Roldan Cuenya, *Angew. Chem., Int. Ed.*, 2017, **56**, 11394–11398.

109 B. Kumar, V. Atla, J. P. Brian, S. Kumari, T. Q. Nguyen, M. Sunkara and J. M. Spurgeon, *Angew. Chem., Int. Ed.*, 2017, **56**, 3645–3649.

110 H. Mistry, A. S. Varela, C. S. Bonifacio, I. Zegkinoglou, I. Sinev, Y. W. Choi, K. Kisslinger, E. A. Stach, J. C. Yang, P. Strasser and B. R. Cuenya, *Nat. Commun.*, 2016, **7**, 12123.

111 F. Scholten, I. Sinev, M. Bernal and B. Roldan Cuenya, *ACS Catal.*, 2019, **9**, 5496–5502.

112 A. Paracchino, J. C. Brauer, J.-E. Moser, E. Thimsen and M. Graetzel, *J. Phys. Chem. C*, 2012, **116**, 7341–7350.

113 R. Kas, R. Kortlever, A. Milbrat, M. T. Koper, G. Mul and J. Baltrusaitis, *Phys. Chem. Chem. Phys.*, 2014, **16**, 12194–12201.

114 D. Ren, Y. Deng, A. D. Handoko, C. S. Chen, S. Malkhandi and B. S. Yeo, *ACS Catal.*, 2015, **5**, 2814–2821.

115 J. Shi, D. Shao, J. Zhang, D. Tan, X. Tan, B. Zhang, B. Han, F. Zhang, L. Liu and X. Cheng, *Chem. Commun.*, 2018, **54**, 5450–5453.

116 D. L. T. Nguyen, M. S. Jee, D. H. Won, H. Jung, H.-S. Oh, B. K. Min and Y. J. Hwang, *ACS Sustainable Chem. Eng.*, 2017, **5**, 11377–11386.

117 D. E. Starr, Z. Liu, M. Havecker, A. Knop-Gericke and H. Bluhm, *Chem. Soc. Rev.*, 2013, **42**, 5833–5857.

118 A. Eilert, F. Cavalca, F. S. Roberts, J. Osterwalder, C. Liu, M. Favaro, E. J. Crumlin, H. Ogasawara, D. Friebel, L. G. Pettersson and A. Nilsson, *J. Phys. Chem. Lett.*, 2017, **8**, 285–290.

119 L. Nguyen, F. F. Tao, Y. Tang, J. Dou and X. J. Bao, *Chem. Rev.*, 2019, **119**, 6822–6905.

**19530** | *J. Mater. Chem. A*, 2021, **9**, 19508–19533

This journal is © The Royal Society of Chemistry 2021

120 E. J. Crumlin, H. Bluhm and Z. Liu, *J. Electron Spectrosc. Relat. Phenom.*, 2013, **190**, 84–92.

121 M. Favaro, J. Yang, S. Nappini, E. Magnano, F. M. Toma, E. J. Crumlin, J. Yano and I. D. Sharp, *J. Am. Chem. Soc.*, 2017, **139**, 8960–8970.

122 L. Cao, Q. Luo, W. Liu, Y. Lin, X. Liu, Y. Cao, W. Zhang, Y. Wu, J. Yang, T. Yao and S. Wei, *Nat. Catal.*, 2018, **2**, 134–141.

123 A. Dutta, A. Kuzume, M. Rahaman, S. Vesztergom and P. Broekmann, *ACS Catal.*, 2015, **5**, 7498–7502.

124 Y. Zhao, X. Chang, A. S. Malkani, X. Yang, L. Thompson, F. Jiao and B. Xu, *J. Am. Chem. Soc.*, 2020, **142**, 9735–9743.

125 X. Chang, Y. Zhao and B. Xu, *ACS Catal.*, 2020, **10**, 13737–13747.

126 K. Kuruvinashetti, Y. Zhang, J. Li and N. Kornienko, *New J. Chem.*, 2020, **44**, 19953–19960.

127 S. Zhu, B. Jiang, W.-B. Cai and M. Shao, *J. Am. Chem. Soc.*, 2017, **139**, 15664–15667.

128 M. Dunwell, Q. Lu, J. M. Heyes, J. Rosen, J. G. Chen, Y. Yan, F. Jiao and B. Xu, *J. Am. Chem. Soc.*, 2017, **139**, 3774–3783.

129 N. P. Finkelstein and R. D. Hancock, *Gold Bull.*, 1974, **7**, 72–77.

130 I. S. Brandt, M. A. Tumelero, S. Pelegrini, G. Zangari and A. A. Pasa, *J. Solid State Electrochem.*, 2017, **21**, 1999–2020.

131 E. McCafferty, in *Introduction to Corrosion Science*, Springer New York, New York, 2010, pp. 95–117, DOI: 10.1007/978-1-4419-0455-3_6.

132 H.-H. Huang, *Metals*, 2016, **6**, 23.

133 B. Beverskog and I. Puigdomenech, *Pourbaix Diagrams for the System Copper-Chlorine at 5-100 °C*, 1998.

134 M. Pourbaix, *Atlas of Electrochemical Equilibria in Aqueous Solutions*, National Association of Corrosion Engineers, Houston, Texas, 1974.

135 D. Kim, S. Lee, J. D. Ocon, B. Jeong, J. K. Lee and J. Lee, *Phys. Chem. Chem. Phys.*, 2015, **17**, 824–830.

136 L. Wang, K. Gupta, J. B. M. Goodall, J. A. Darr and K. B. Holt, *Faraday Discuss.*, 2017, **197**, 517–532.

137 Y. Lum and J. W. Ager, *Angew. Chem., Int. Ed.*, 2018, **57**, 551–554.

138 M. S. Jee, H. Kim, H. S. Jeon, K. H. Chae, J. Cho, B. K. Min and Y. J. Hwang, *Catal. Today*, 2017, **288**, 48–53.

139 F. Cavalca, R. Ferragut, S. Aghion, A. Eilert, O. Diaz-Morales, C. Liu, A. L. Koh, T. W. Hansen, L. G. M. Pettersson and A. Nilsson, *J. Phys. Chem. C*, 2017, **121**, 25003–25009.

140 S. Lee, D. Kim and J. Lee, *Angew. Chem., Int. Ed.*, 2015, **54**, 14701–14705.

141 R. Imani, Z. Qiu, R. Younesi, M. Pazoki, D. L. A. Fernandes, P. D. Mitev, T. Edvinsson and H. Tian, *Nano Energy*, 2018, **49**, 40–50.

142 X. An, S. Li, A. Yoshida, T. Yu, Z. Wang, X. Hao, A. Abudula and G. Guan, *ACS Appl. Mater. Interfaces*, 2019, **11**, 42114–42122.

143 K. Ye, Z. Zhou, J. Shao, L. Lin, D. Gao, N. Ta, R. Si, G. Wang and X. Bao, *Angew. Chem., Int. Ed.*, 2020, **59**, 4814–4821.

144 Y. W. Choi, F. Scholten, I. Sinev and B. Roldan Cuenya, *J. Am. Chem. Soc.*, 2019, **141**, 5261–5266.

145 Q. Zhu, D. Yang, H. Liu, X. Sun, C. Chen, J. Bi, J. Liu, H. Wu and B. Han, *Angew. Chem., Int. Ed.*, 2020, **59**, 8896–8901.

146 X. Zheng, P. De Luna, F. P. García de Arquer, B. Zhang, N. Becknell, M. B. Ross, Y. Li, M. N. Banis, Y. Li, M. Liu, O. Voznyy, C. T. Dinh, T. Zhuang, P. Stadler, Y. Cui, X. Du, P. Yang and E. H. Sargent, *Joule*, 2017, **1**, 794–805.

147 M. Asadi, K. Kim, C. Liu, A. V. Addepalli, P. Abbasi, P. Yasaei, P. Phillips, A. Behranginia, J. M. Cerrato, R. Haasch, P. Zapol, B. Kumar, R. F. Klie, J. Abiade, L. A. Curtiss and A. Salehi-Khojin, *Science*, 2016, **353**, 467–470.

148 A. Aljabour, H. Coskun, X. Zheng, M. G. Kibria, M. Strobel, S. Hild, M. Kehrer, D. Stifter, E. H. Sargent and P. Stadler, *ACS Catal.*, 2019, **10**, 66–72.

149 P. Abbasi, M. Asadi, C. Liu, S. Sharifi-Asl, B. Sayahpour, A. Behranginia, P. Zapol, R. Shahbazian-Yassar, L. A. Curtiss and A. Salehi-Khojin, *ACS Nano*, 2017, **11**, 453–460.

150 M. Asadi, B. Kumar, A. Behranginia, B. A. Rosen, A. Baskin, N. Repnin, D. Pisasale, P. Phillips, W. Zhu, R. Haasch, R. F. Klie, P. Kral, J. Abiade and A. Salehi-Khojin, *Nat. Commun.*, 2014, **5**, 4470.

151 C. Li, G. Shen, R. Zhang, D. Wu, C. Zou, T. Ling, H. Liu, C. Dong and X.-W. Du, *J. Mater. Chem. A*, 2019, **7**, 1418–1423.

152 F. P. Garcia de Arquer, O. S. Bushuyev, P. De Luna, C. T. Dinh, A. Seifitokaldani, M. I. Saidaminov, C. S. Tan, L. N. Quan, A. Proppe, M. G. Kibria, S. O. Kelley, D. Sinton and E. H. Sargent, *Adv. Mater.*, 2018, **30**, 1802858.

153 Q. Zhu, X. Sun, D. Yang, J. Ma, X. Kang, L. Zheng, J. Zhang, Z. Wu and B. Han, *Nat. Commun.*, 2019, **10**, 3851.

154 R. Wang, H. Haspel, A. Pustovarenko, A. Dikhtiarenko, A. Russkikh, G. Shterk, D. Osadchii, S. Ould-Chikh, M. Ma, W. A. Smith, K. Takanabe, F. Kapteijn and J. Gascon, *ACS Energy Lett.*, 2019, **4**, 2024–2031.

155 P. Lamagni, M. Miola, J. Catalano, M. S. Hvid, M. A. H. Mamakhel, M. Christensen, M. R. Madsen, H. S. Jeppesen, X. M. Hu, K. Daasbjerg, T. Skrydstrup and N. Lock, *Adv. Funct. Mater.*, 2020, **30**, 1910408.

156 T. Fan, Q. Wu, Z. Yang, Y. Song, J. Zhang, P. Huang, Z. Chen, Y. Dong, W. Fang and X. Yi, *ChemSusChem*, 2020, **13**, 2677–2683.

157 D. Gao, I. Zegkinoglou, N. J. Divins, F. Scholten, I. Sinev, P. Grosse and B. Roldan Cuenya, *ACS Nano*, 2017, **11**, 4825–4831.

158 C. Liu, M. P. Lourenço, S. Hedström, F. Cavalca, O. Diaz-Morales, H. A. Duarte, A. Nilsson and L. G. M. Pettersson, *J. Phys. Chem. C*, 2017, **121**, 25010–25017.

159 Z. Gu, N. Yang, P. Han, M. Kuang, B. Mei, Z. Jiang, J. Zhong, L. Li and G. Zheng, *Small Methods*, 2019, **3**, 1800449.

160 P. Yang, Z. J. Zhao, X. Chang, R. Mu, S. Zha, G. Zhang and J. Gong, *Angew. Chem., Int. Ed.*, 2018, **57**, 7724–7728.

161 L. Qi, S. Liu, W. Gao and Q. Jiang, *J. Phys. Chem. C*, 2018, **122**, 5472–5480.

162 X. Zhi, Y. Jiao, Y. Zheng, K. Davey and S.-Z. Qiao, *J. Mater. Chem. A*, 2021, **9**, 6345–6351.

This journal is © The Royal Society of Chemistry 2021

*J. Mater. Chem. A*, 2021, **9**, 19508–19533 | **19531**

163 W. Ju, A. Bagger, G. P. Hao, A. S. Varela, I. Sinev, V. Bon, B. Roldan Cuenya, S. Kaskel, J. Rossmeisl and P. Strasser, *Nat. Commun.*, 2017, **8**, 944.

164 D. Liu, Y. Liu and M. Li, *J. Phys. Chem. C*, 2020, **124**, 6145–6153.

165 A. Dutta, M. Rahaman, N. C. Luedi, M. Mohos and P. Broekmann, *ACS Catal.*, 2016, **6**, 3804–3814.

166 J. Gao, C. Zhu, M. Zhu, Y. Fu, H. Huang, Y. Liu and Z. Kang, *ACS Sustainable Chem. Eng.*, 2019, **7**, 3536–3543.

167 L. Fan, Z. Xia, M. Xu, Y. Lu and Z. Li, *Adv. Funct. Mater.*, 2018, **28**, 1706289.

168 M. K. Kim, H. J. Kim, H. Lim, Y. Kwon and H. M. Jeong, *Electrochim. Acta*, 2019, **306**, 28–34.

169 D. Wu, J. Liu, Y. Liang, K. Xiang, X. Z. Fu and J. L. Luo, *ChemSusChem*, 2019, **12**, 4700–4707.

170 S. D. Giri, S. M. Mahajani, A. K. Suresh and A. Sarkar, *Mater. Res. Bull.*, 2020, **123**, 110702.

171 Y. Yoon, A. S. Hall and Y. Surendranath, *Angew. Chem., Int. Ed.*, 2016, **55**, 15282–15286.

172 A. S. Hall, Y. Yoon, A. Wuttig and Y. Surendranath, *J. Am. Chem. Soc.*, 2015, **137**, 14834–14837.

173 C. Chen, B. Zhang, J. Zhong and Z. Cheng, *J. Mater. Chem. A*, 2017, **5**, 21955–21964.

174 S. Suter and S. Haussener, *Energy Environ. Sci.*, 2019, **12**, 1668–1678.

175 F. Calle-Vallejo and M. T. Koper, *Angew. Chem., Int. Ed.*, 2013, **52**, 7282–7285.

176 J. H. Montoya, C. Shi, K. Chan and J. K. Norskov, *J. Phys. Chem. Lett.*, 2015, **6**, 2032–2037.

177 M. S. Jee, H. S. Jeon, C. Kim, H. Lee, J. H. Koh, J. Cho, B. K. Min and Y. J. Hwang, *Appl. Catal., B*, 2016, **180**, 372–378.

178 W. J. Dong, C. J. Yoo and J.-L. Lee, *ACS Appl. Mater. Interfaces*, 2017, **9**, 43575–43582.

179 J. J. Velasco-Velez, C. H. Chuang, D. Gao, Q. Zhu, D. Ivanov, H. S. Jeon, R. Arrigo, R. V. Mom, E. Stotz, H. L. Wu, T. E. Jones, B. Roldan Cuenya, A. Knop-Gericke and R. Schlogl, *ACS Catal.*, 2020, **10**, 11510–11518.

180 A. Dutta, I. Z. Montiel, R. Erni, K. Kiran, M. Rahaman, J. Drnec and P. Broekmann, *Nano Energy*, 2020, **68**, 104331.

181 P. Wang, M. Qiao, Q. Shao, Y. Pi, X. Zhu, Y. Li and X. Huang, *Nat. Commun.*, 2018, **9**, 4933.

182 S. C. Abeyweera, J. Yu, J. P. Perdew, Q. Yan and Y. Sun, *Nano Lett.*, 2020, **20**, 2806–2811.

183 A. Verdaguer-Casadevall, C. W. Li, T. P. Johansson, S. B. Scott, J. T. McKeown, M. Kumar, I. E. Stephens, M. W. Kanan and I. Chorkendorff, *J. Am. Chem. Soc.*, 2015, **137**, 9808–9811.

184 X. Feng, K. Jiang, S. Fan and M. W. Kanan, *ACS Cent. Sci.*, 2016, **2**, 169–174.

185 R. G. Mariano, M. Kang, O. J. Wahab, I. J. McPherson, J. A. Rabinowitz, P. R. Unwin and M. W. Kanan, *Nat. Mater.*, 2021, **20**, 1000–1006.

186 J. J. Velasco-Velez, R. V. Mom, L. E. Sandoval-Diaz, L. J. Falling, C. H. Chuang, D. Gao, T. E. Jones, Q. Zhu, R. Arrigo, B. Roldan Cuenya, A. Knop-Gericke, T. Lunkenbein and R. Schlogl, *ACS Energy Lett.*, 2020, **5**, 2106–2111.

187 T. Cheng, H. Xiao and W. A. Goddard, *J. Am. Chem. Soc.*, 2017, **139**, 11642–11645.

188 L. Li, D.-K. Ma, F. Qi, W. Chen and S. Huang, *Electrochim. Acta*, 2019, **298**, 580–586.

189 Y. Hori, I. Takahashi, O. Koga and N. Hoshi, *J. Phys. Chem. B*, 2002, **106**, 15–17.

190 G. L. De Gregorio, T. Burdyny, A. Loiudice, P. Iyengar, W. A. Smith and R. Buonsanti, *ACS Catal.*, 2020, **10**, 4854–4862.

191 W. Luc, X. Fu, J. Shi, J.-J. Lv, M. Jouny, B. H. Ko, Y. Xu, Q. Tu, X. Hu, J. Wu, Q. Yue, Y. Liu, F. Jiao and Y. Kang, *Nat. Catal.*, 2019, **2**, 423–430.

192 S. Liu, H. Tao, L. Zeng, Q. Liu, Z. Xu, Q. Liu and J. L. Luo, *J. Am. Chem. Soc.*, 2017, **139**, 2160–2163.

193 H. Won da, H. Shin, J. Koh, J. Chung, H. S. Lee, H. Kim and S. I. Woo, *Angew. Chem., Int. Ed.*, 2016, **55**, 9297–9300.

194 Y. G. Kim, J. H. Baricuatro, A. Javier, J. M. Gregoire and M. P. Soriaga, *Langmuir*, 2014, **30**, 15053–15056.

195 Y.-G. Kim, A. Javier, J. H. Baricuatro and M. P. Soriaga, *Electrocatalysis*, 2016, **7**, 391–399.

196 C. F. Tsang, A. C. Javier, Y.-G. Kim, J. H. Baricuatro, K. D. Cummins, J. Kim, G. Jerkiewicz, J. C. Hemminger and M. P. Soriaga, *J. Electrochem. Soc.*, 2018, **165**, J3350–J3354.

197 F. S. Roberts, K. P. Kuhl and A. Nilsson, *Angew. Chem., Int. Ed.*, 2015, **54**, 5179–5182.

198 Y. Wang, Z. Wang, C.-T. Dinh, J. Li, A. Ozden, M. Golam Kibria, A. Seifitokaldani, C.-S. Tan, C. M. Gabardo, M. Luo, H. Zhou, F. Li, Y. Lum, C. McCallum, Y. Xu, M. Liu, A. Proppe, A. Johnston, P. Todorovic, T.-T. Zhuang, D. Sinton, S. O. Kelley and E. H. Sargent, *Nat. Catal.*, 2019, **3**, 98–106.

199 D. Kim, C. S. Kley, Y. Li and P. Yang, *Proc. Natl. Acad. Sci. U. S. A.*, 2017, **114**, 10560–10565.

200 M. M. Sartin, Z. Yu, W. Chen, F. He, Z. Sun, Y.-X. Chen and W. Huang, *J. Phys. Chem. C*, 2018, **122**, 26489–26498.

201 R. M. Aran-Ais, R. Rizo, P. Grosse, G. Algara-Siller, K. Dembele, M. Plodinec, T. Lunkenbein, S. W. Chee and B. R. Cuenya, *Nat. Commun.*, 2020, **11**, 3489.

202 T. Moller, F. Scholten, T. N. Thanh, I. Sinev, J. Timoshenko, X. Wang, Z. Jovanov, M. Gliech, B. Roldan Cuenya, A. S. Varela and P. Strasser, *Angew. Chem., Int. Ed.*, 2020, **59**, 17974–17983.

203 A. S. Malkani, M. Dunwell and B. Xu, *ACS Catal.*, 2018, **9**, 474–478.

204 Y. Hori, O. Koga, Y. Watanabe and T. Matsuo, *Electrochim. Acta*, 1998, **44**, 1389–1395.

205 N. Hoshi, M. Kato and Y. Hori, *J. Electroanal. Chem.*, 1997, **440**, 283–286.

206 S. Popovic, M. Smiljanic, P. Jovanovic, J. Vavra, R. Buonsanti and N. Hodnik, *Angew. Chem., Int. Ed.*, 2020, **59**, 14736–14746.

207 Y. Hori, H. Konishi, T. Futamura, A. Murata, O. Koga, H. Sakurai and K. Oguma, *Electrochim. Acta*, 2005, **50**, 5354–5369.

208 A. Wuttig and Y. Surendranath, *ACS Catal.*, 2015, **5**, 4479–4484.

209 J. He, A. Huang, N. J. J. Johnson, K. E. Dettelbach, D. M. Weekes, Y. Cao and C. P. Berlinguette, *Inorg. Chem.*, 2018, **57**, 14624–14631.

210 C. T. Dinh, T. Burdyny, M. G. Kibria, A. Seifitokaldani, C. M. Gabardo, F. P. García de Arquer, A. Kiani, J. P. Edwards, P. De Luna, O. S. Bushuyev, C. Zou, R. Quintero-Bermudez, Y. Pang, D. Sinton and E. H. Sargent, *Science*, 2018, **360**, 783–787.

211 P. Grosse, D. Gao, F. Scholten, I. Sinev, H. Mistry and B. Roldan Cuenya, *Angew. Chem., Int. Ed.*, 2018, **57**, 6192–6197.

212 J. Huang, N. Hormann, E. Oveisi, A. Loiudice, G. L. De Gregorio, O. Andreussi, N. Marzari and R. Buonsanti, *Nat. Commun.*, 2018, **9**, 3117.

213 X. Yuan, S. Chen, D. Cheng, L. Li, W. Zhu, D. Zhong, Z. J. Zhao, J. Li, T. Wang and J. Gong, *Angew. Chem., Int. Ed.*, 2021, **60**, 15344–15347.

214 Y. Zhang, L. Hu and W. Han, *J. Mater. Chem. A*, 2018, **6**, 23610–23620.

215 C. S. Le Duff, M. J. Lawrence and P. Rodriguez, *Angew. Chem., Int. Ed.*, 2017, **56**, 12919–12924.

216 A. Engelbrecht, M. Hämmerle, R. Moos, M. Fleischer and G. Schmid, *Electrochim. Acta*, 2017, **224**, 642–648.

217 K. Obata and K. Takanabe, *Angew. Chem., Int. Ed.*, 2018, **57**, 1616–1620.

218 D. V. Esposito, *ACS Catal.*, 2017, **8**, 457–465.

219 N. Y. Labrador, E. L. Songcuan, C. De Silva, H. Chen, S. J. Kurdziel, R. K. Ramachandran, C. Detavernier and D. V. Esposito, *ACS Catal.*, 2018, **8**, 1767–1778.

220 J. E. Robinson, N. Y. Labrador, H. Chen, B. E. Sartor and D. V. Esposito, *ACS Catal.*, 2018, **8**, 11423–11434.

221 A. A. Bhardwaj, J. G. Vos, M. E. S. Beatty, A. F. Baxter, M. T. M. Koper, N. Y. Yip and D. V. Esposito, *ACS Catal.*, 2021, **11**, 1316–1330.

222 P. F. Liu, M. Y. Zu, L. R. Zheng and H. G. Yang, *Chem. Commun.*, 2019, **55**, 12392–12395.

223 C. Cao, D.-D. Ma, J.-F. Gu, X. Xie, G. Zeng, X. Li, S.-G. Han, Q.-L. Zhu, X.-T. Wu and Q. Xu, *Angew. Chem., Int. Ed.*, 2020, **59**, 15014–15020.

224 Z.-Q. Liang, T.-T. Zhuang, A. Seifitokaldani, J. Li, C.-W. Huang, C.-S. Tan, Y. Li, P. De Luna, C. T. Dinh, Y. Hu, Q. Xiao, P.-L. Hsieh, Y. Wang, F. Li, R. Quintero-Bermudez, Y. Zhou, P. Chen, Y. Pang, S.-C. Lo, L.-J. Chen, H. Tan, Z. Xu, S. Zhao, D. Sinton and E. H. Sargent, *Nat. Commun.*, 2018, **9**, 3828.

This journal is © The Royal Society of Chemistry 2021

*J. Mater. Chem. A*, 2021, **9**, 19508–19533 | **19533**